Title
DIFFERENTIAL DISTRIBUTION OF CHARGE-EXCHANGE AND INELASTIC NEUTRONS IN n--p INTERACTIONS AT 313 AND 371 MeV

Author
Lind, D.L.

Publication Date
1964-07-01

DISCLAIMER

UCRL-11435

UNIVERSITY OF CALIFORNIA

Lawrence Radiation Laboratory
Berkeley, California

AEC Contract No. W-7405-eng-48

DIFFERENTIAL DISTRIBUTION OF CHARGE-EXCHANGE AND INELASTIC NEUTRONS IN π^--p INTERACTIONS AT 313 AND 371 MeV

Don Leslie Lind

(Ph. D. Thesis)

July 1, 1964

Printed in USA. Price $1.25. Available from the
Office of Technical Services
U. S. Department of Commerce
Washington 25, D.C.

DIFFERENTIAL DISTRIBUTION OF CHARGE-EXCHANGE AND INELASTIC NEUTRONS IN π^--p INTERACTIONS AT 313 AND 371 MeV

Contents

DIFFERENTIAL DISTRIBUTION OF CHARGE-EXCHANGE AND INELASTIC NEUTRONS IN π^--p INTERACTIONS AT 313 AND 371 MeV

Don Leslie Lind

Lawrence Radiation Laboratory
University of California
Berkeley, California

July 1, 1964

ABSTRACT

Neutron distributions from the charge-exchange (π^0n) and inelastic modes ($\pi^0\pi^0$n, $\pi^+\pi^-$n) of the π^--p interaction are investigated at 313 and 371 MeV. The pion beam of the Berkeley 184-inch synchrocyclotron is focused on a liquid hydrogen target. The scattered neutrons are detected in blocks of plastic scintillator surrounded by anticoincidence counters. Their time-of-flight distribution is determined electronically. Elastic and inelastic neutrons are separated in the all-neutral final states by this time-of-flight information.

The charge-exchange differential cross section is least-squares fit with a Legendre expansion of the form

$$\frac{d\sigma}{d\Omega^*}(\cos\theta^*_{\pi^0}) = \sum_{\ell=0}^{N} a_\ell P_\ell(\cos\theta^*_{\pi^0})$$

with the following results (in mb/sr):

T_{π^-}	a_0	a_1	a_2	a_3
313	1.21±0.03	1.92±0.06	1.61±0.06	0.48±0.05
371	0.89±0.02	1.57±0.04	1.13±0.04	0.38±0.03

The charged-mode inelastic-neutron ($\pi^+\pi^-n$) distribution has a marked enhancement at the lowest c.m. neutron energies (highest two-pion kinetic energy). There is no clear evidence of an ABC effect. The neutral mode ($\pi^0\pi^0n$) distribution is inconclusive.

I. INTRODUCTION

The motivation for an experiment to detect neutrons arising in $\pi^- p$ collisions in the 300 to 400-MeV energy range came from interest in both classes of neutron final-states expected from this reaction. The elastic neutrons ($n\pi^0$) would provide a technique for measuring the differential cross section for this charge-exchange reaction, these measurements could clear up some questions concerning the existing data. In addition, study of the inelastic neutrons ($n\pi^0\pi^0$ and $n\pi^-\pi^+$) would provide information about the two-pion interaction in the isotopic state I = 0. The small contribution to the neutron yield from the γn final state could be properly accounted for with a detailed balance calculation.

A. Elastic Neutrons

The interaction of pions and nucleons is of fundamental importance in nuclear physics since a major component of nuclear force is believed to result from the interchange of pions by the nucleons in the nucleus. For this reason, the pion-nucleon interaction has been studied for some time, usually by means of scattering experiments involving charged pions and protons. Such pion-nucleon scattering data can be analyzed in terms of partial waves, for which the scattering amplitudes are expanded in a series of terms, each term corresponding to a definite angular momentum and parity state of the pion-nucleon system. These partial-wave expansions are parameterized with the phase shifts that measure the strength of the interaction in each angular-momentum and isotopic-spin state. Theoretical predictions concerning the pion-nucleon system can then be compared with this phase-shift analysis.

For the simple case of elastic scattering, the amplitude of the quantum mechanical wave representing the scattered particles has the form

$$f(\theta)\,\frac{\exp(ikr)}{r}$$

at large distances r from the target. The particle momentum is k in units of $\hbar$, and

$$f(\theta) = \sum_{\ell} \frac{(2\ell+1)}{k} P_{\ell}(\cos\theta) \exp(i\delta_{\ell}) \sin\delta_{\ell} .$$

The differential cross section, $d\sigma/d\Omega$, is equal to $|f(\theta)|^2$. The parameters δ_{ℓ} are the phase shifts, where ℓ represents all the quantum numbers needed to specify each state in the partial-wave expansion, usually angular momentum and isotopic spin. The phase shifts measure the angle by which the scattering potential changes the phase of the scattered wave with respect to the incoming wave. If the scattering is not purely elastic, δ_{ℓ} will be complex with its imaginary part representing the amount of absorption that occurs in the reaction.

The isotopic-spin state for $\pi^+ p$ scattering is pure $I = 3/2$, whereas the $\pi^- p$ system is formed from a superposition of $I = 3/2$ and $I = 1/2$ states. This fact evidences itself in the partial-wave analysis by the amplitudes for $\pi^- p$ elastic scattering being proportional to

$$(1/3)M_{3/2} + (2/3)M_{1/2}$$

and the amplitudes for $\pi^- p$ charge-exchange scattering bring proportional to

$$(\sqrt{2}/3)M_{3/2} - (\sqrt{2}/3)\, M_{1/2} ,$$

where $M_{3/2}$ and $M_{1/2}$ are the matrix elements for the transitions of the $I = 3/2$ and $1/2$ states, respectively. Since the cross section for charge-exchange scattering is proportional to the square of an amplitude formed from the difference of the two isotopic spin states, the measurement of this cross section can provide a separate and sensitive contribution in determining the phase shifts corresponding to these isotopic-spin states.

When a program of phase-shift analysis was contemplated in the energy region of the higher pion-nucleon resonances (600 to 900 MeV), it seemed obvious that a hopelessly large number of solutions could equally well represent the data. Therefore to reduce the number of phase-shift solutions--hopefully to a single correct solution--the necessary first step seemed to be to determine a unique set of phase

shifts that accurately represented the data at some lower energy at which a relatively few angular-momentum states could contribute. Then a continuous solution could be traced into the higher energy regions. This is the program now being forwarded by a number of investigators.

Three hundred and ten MeV seemed to be the desirable incident-pion energy at which to try to determine an unambiguous-phase-shift solution. Classically, D waves (up to and including $\ell = 2$) are expected to become noticeable by this energy. Foote et al.[1] and Rogers et al.[2] had made a very accurate determination of π^+p differential cross sections and recoil-proton polarization at this energy. Some π^-p differential cross section and polarization data had been obtained at 307 MeV by Zinov and Korenchenko,[3] and Vasilevskiĭ and Vishnyakov.[4] However these data were not sufficiently accurate for good phase-shift analysis. Therefore Rugge and Vik[5] proceeded to measure the π^-p differential cross sections and polarization with an accuracy corresponding to the π^+p work of Foote and Rogers.

One additional set of data was available for the phase-shift analysis, since Caris et al.[6] had measured the charge-exchange differential cross section at 317 MeV. However when the Caris data were compared with charge-exchange distributions predicted by phase-shift solutions determined with the elastic-scattering differential-cross-section and polarization data,[7] it was apparent that there was considerable deviation at the backward pion angles. It appeared that this charge-exchange information was not quite consistent with the large amount of elastic-scattering data.

The charge-exchange distribution had not been measured directly since, because of the extremely short lifetime of the π^0 meson (2.2×10^{-16} sec), it did not emerge from the hydrogen target. Only the gamma rays into which the π^0 decays could therefore be detected. From this observed gamma-ray spectrum, the π^0 angular distribution had to be deduced by relating the Legendre coefficients that fit the γ-ray distribution to the Legendre expansion for the π^0 distribution.[6,8] This procedure, of course, was not as satisfying as if the angular distribution of one of the reaction products could have been observed directly.

At the time when the charge-exchange data by Caris et al. were analyzed, not even the total cross sections for the inelastic processes that contribute to the observed γ rays ($\pi^0\pi^0 n$ and $\pi^-\pi^0 p$) were well known. They were assumed to be equal to that of the $\pi^-\pi^+ n$ reaction measured by Perkins.[9] Subsequent data have shown this to be incorrect.[10] Although the total cross section for these inelastic processes is small compared to that of the charge-exchange data being corrected, at backward pion angles the differential cross sections are very nearly equal. Thus a small uncertainty in the effect of the γ rays from the inelastic processes could significantly alter the final angular distribution. And it was at these same backward angles that the phase-shift predictions of Vik and Rugge departed most from the charge-exchange data of Caris. In addition, charge-exchange data taken by Kurz[10] at 374 MeV appeared to differ sufficiently from corresponding observations made by Caris to be in significant disagreement.

Sufficient doubt had been raised concerning the charge-exchange data available in this energy region that it was decided to attempt to measure the differential cross section by observing the only directly accessible final-state particle--the neutron. Neutral particles are, in general, more difficult to observe than charged particles, but this experiment presented an additional complication. The elastic and inelastic neutrons were to be separated by detecting a difference in the time it took them to traverse a measured path length. This would require an electronics system with an over-all time resolution of the order of 1.5 nsec. This presented a considerable challenge, but it appeared that such charge-exchange data would certainly be needed to complete the phase-shift-analysis program.

B. Inelastic Neutrons

While making measurements of the momentum spectra of He^3 and H^3 nuclei produced in the collisions of high-energy protons with deuterium, Abashian et al. reported detecting an anomalous bump in the He^3 momentum spectrum (the so-called ABC effect).[11,12] In the reaction $p + d \rightarrow He^3 + 2\pi$, the two-pion system corresponds to a mixture of isotopic-spin eigenstates having I = 0 and I = 1. But in the corresponding H^3 final state, the two-pion system occurs only with I = 1. Thus by appropriately subtracting the I = 1 state from the He^3 spectrum, they showed that the anomaly existed only in the I = 0 state.

These authors concluded that the anomaly was an enhancement in the two-pion production in the I = 0 state, and could be explained as a strongly attractive low-energy pion-pion interaction.[12] A scattering length of $2 \pm 1\ \mu^{-1}$ was assigned.

However two other groups at Berkeley[10,13] had looked at two-pion final states ($\pi^-\pi^+n$ and $\pi^0\pi^0n$) in pion-nucleon collisions and had not observed any clear evidence for such a two-pion interaction. Both of these states should have exhibited any I = 0 two-pion enhancement since the first is a mixture of eigenstates having I = 0, 1, and 2, and the second is composed of I = 0 and 2. Instead, they had observed a peaking of the neutron-energy distributions that corresponded to the maximum kinematically possible relative two-pion energy. This new effect was observed in both final states with both counter and bubble chamber techniques.

These developments indicated the desirability of more measurements on the I = 0 two-pion system. Since the inelastic neutrons that we had to identify and separate from the charge-exchange differential-cross-section data arose from precisely these same two-pion final states, we could readily obtain such data. We could conveniently carry out the two investigations simultaneously, using the same experimental equipment.

Thus with this double motivation, we proceeded with the investigation of neutrons arising from π^-p collisions at 313 and 371 MeV.

The lower energy was chosen to correspond to the energy at which the Segrè group was working. The higher energy approaches the practical upper limit for separating inelastic neutrons by time of flight and was selected so that comparison could be made with data taken by Kurz.

II. EXPERIMENTAL METHOD

The collision of a pion from a 313 or 371 MeV beam and a proton in a liquid hydrogen target provides sufficient energy to open some of the inelastic channels of the πN system with the production of an additional final-state pion. Although the higher of these energies is above the threshold for the production of two extra pions, these contributions are assumed to be negligibly small. Thus the experimental task involved in the investigation of $\pi^- p$ interactions in this energy range is to detect and separate the products of the following reactions.

$\pi^- + p \rightarrow \pi^- + p$	elastic scattering	(1)
$\pi^- + p \rightarrow \pi^0 + n$	charge exchange	(2)
$\pi^- + p \rightarrow \gamma + n$	radiative absorption	(3)
$\pi^- + p \rightarrow \pi^0 + \pi^0 + n$		(4)
$\pi^- + p \rightarrow \pi^- + \pi^+ + n$	pion production	(5)
$\pi^- + p \rightarrow \pi^- + \pi^0 + p$		(6)
$\pi^- + p \rightarrow \pi^- + \gamma + p$	nuclear bremsstrahlung	(7)

A detector accepting only neutral particles will signal the presence of a neutron (since gamma rays can be distinguished from neutrons, as we show) and will eliminate reactions (1), (6), and (7). The cross section for radiative absorption (3) is small compared to other neutron sources, so these neutrons can be treated as a mathematical correction to the data. Next, if the hydrogen target is surrounded by a scintillation counter that will detect any charged pions in coincidence with a neutron, these reactions can be labelled as (5) and counted separately. They are analyzed with the two-pion ($I = 0$) interaction in mind.

Now we are left only with reactions (2) and (4) to separate. The inelastic neutrons of reaction (4) emerge from the target with a spectrum of energies. At a fixed lab-system angle, enough energy is removed from the reaction as the rest mass of the second pion that the highest kinetic energy available to the inelastic neutrons is below the unique energy of the elastically scattered charge-exchange neutrons [Eq. (2)]. Thus the arrival of these groups of neutrons at a detector is

separated by a small increment of time. When the neutrons' flight path was a few meters and we paid very careful attention to the required time-of-flight measurements, we were able to clearly distinguish between the elastic and the inelastic neutrons. In addition, the gamma rays that registered in the neutron counter--both the direct final-state products and those arising from the various decaying π^0's--are easily separated from the neutrons, since they arrive several nanoseconds sooner than the fastest neutrons.

This then, in general, was our experimental technique. Now let us look in detail at the components used in carrying it out.

A. Pion Beam

1. Beam Design

The negative pion beam was produced in the reaction $p + n \rightarrow p + p + \pi^-$ when the internal 732-MeV proton beam of the Berkeley 184-inch synchrocyclotron struck an internal beryllium target. This target had a cross section 1/2 in. in the radial direction by 2 in. in the vertical direction and was 2-in. thick in the beam direction. Because the phase space for this reaction decreases rapidly as a function of angle, production of high-energy-pion beams is limited to angles close to 0 deg.

These pions were deflected outwardly by the magnetic field of the cyclotron, and passed through a thin aluminum window in the vacuum tank and into the 8-in. aperture of the doublet quadrupole magnet Q_1 (see Fig. 1). The trajectory of such pions was calculated by the IBM 709-7090 FORTRAN program CYCLOTRON ORBITS,[14] which uses measured values of the cyclotron magnetic field to integrate the equations of motion of the particle. Previous experience indicated that the maximum pion flux occurs where the orbits of the internal proton beam are nearly 82 in. in radius. We set the Be target at this radius and required that the calculated pion trajector pass through the center of the 8-ft.-long iron collimator known as the meson wheel. This fixed both the azimuthal position of the Be target and the angular position of the

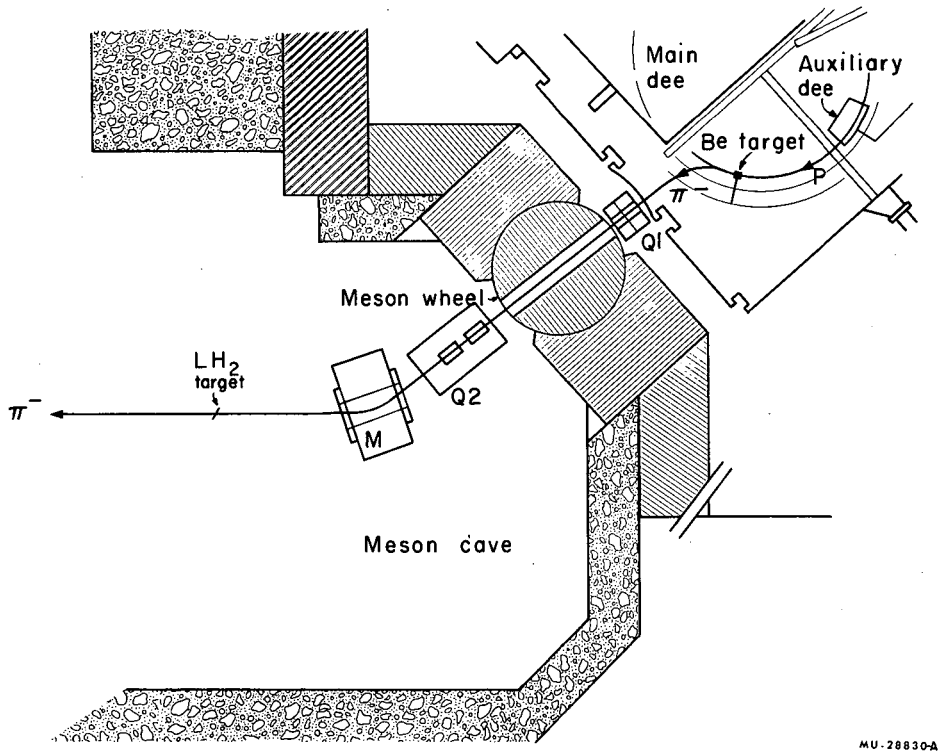

Fig. 1. Plan view of the meson cave in the 184-inch cyclotron showing the magnetic system for the pion beam. Detail of the target area is shown in Fig. 6.

meson wheel. Both space requirements and optimization of the beam focus dictated that the external doublet quadrupole magnet Q_2 and the bending magnet M should be located as near the meson wheel as possible. Thus the physical arrangement of the beam system was chosen.

The magnetic-field parameters of the beam-transport system were determined with an IBM 709-7090 FORTRAN program called OPTIK.[15] This program treats a high-energy-particle beam analogously to a geometrical optical beam. The beam is represented as a 6-dimensional vector--the lateral and angular displacements both vertically and horizontally from the beam line, the momentum spread of the beam, and a projection operator that accounts for particles of different mass and thus different velocities in a monochromatic beam. The effect of each element of the system (bending magnet, quadrupole, etc.) on this vector is given by a matrix acting on the vector. In such a problem the field of the cyclotron can be simulated by three elements: a field-free region, a bending magnet, and another field-free region. A matrix combining these elements was used as the first component of the magnet system.

The requirement that the beam must be parallel as it passed through the meson wheel determined the field strengths for the two elements of the internal quadrupole Q_1. The polarity of Q_1 was set opposite to that of the external quadrupole Q_2 in order to maximize the solid angle for acceptance of the beam. Quadrupole Q_2 was set so as to refocus this parallel beam at the target position. The angle of bend for the selected pion momenta in the 36×18-in. magnet M (θ_2 in Fig. 2) and the hydrogen-target position (L in Fig. 2) were chosen so that the momentum dispersion for the analyzing magnet M exactly compensated the dispersion in the rest of the system. In this way the required magnetic fields for all elements of the system were calculated.

2. Measured Properties

The calculated parameters of the system were verified empirically when the system was assembled. The current required to produce the desired angle of bend was checked by the suspended-wire technique.[16]

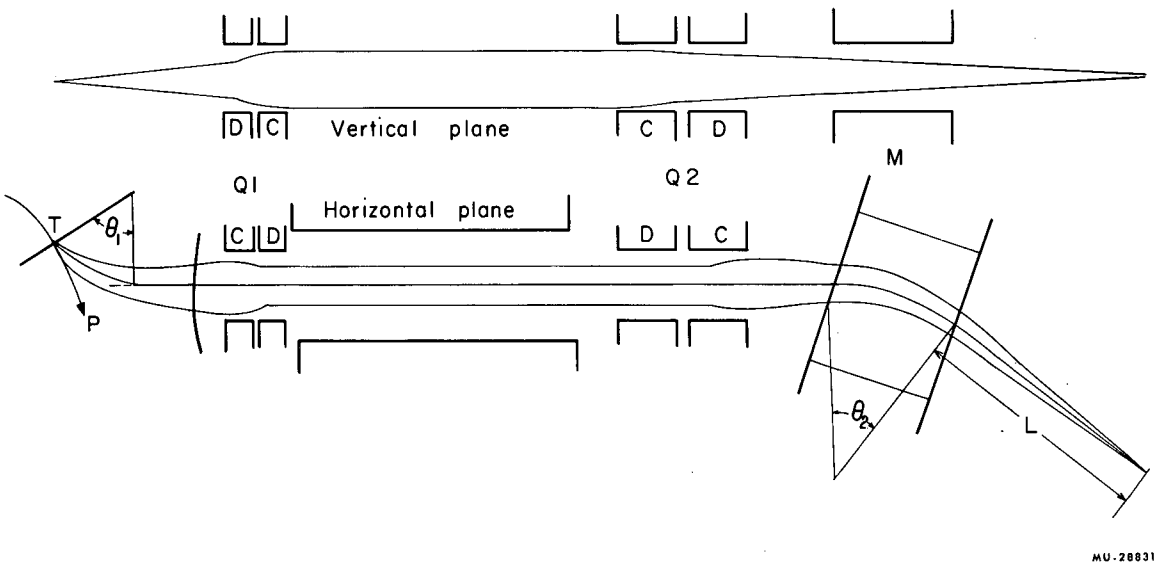

Fig. 2. Beam-optics diagram.
C = convergent quadrupole element
D = divergent quadrupole element
T = internal Be target
P = internal proton beam
θ_1 = 67 deg
θ_2 = 45 deg
L = 88.5 in

Here the beam is simulated by a taut, flexible wire in which the current corresponds to the momentum of the beam, and the tension to the magnetic rigidity of the beam particles. The quadrupoles were tuned to give the best beam profiles at the final image. The final settings agreed well with those calculated by OPTIK. Figure 3 shows the profiles of the 371-MeV beam after the 3/8-in. rectangular resolution function of the beam detector[17] was unfolded from the observed profiles. Similar profiles were obtained for the 313-MeV beam. To reduce the widening of the profiles by multiple Coulomb scattering of the pions by air, the beam path was maintained in an atmosphere of helium gas from the entrance of Q_2 to the exit of M.

The average energy and the energy spread of the beam were determined by the integral-range method. Transmission was measured as a function of copper-absorber thickness by recording the ratio of particles entering the absorber with those emerging beyond it. Figure 4 shows the integral-range curve at 313 MeV. The 371-MeV range curve was similar. Point A is the break between the pion-absorption-loss curve and the actual stopping of pions. Pions stopped between points A and B. Point B marks the high-energy end of the pion-stopping range and the low-energy end of the muon-stopping range. Beyond point C only electrons penetrate through the absorber. The difference between points A and B represents the energy spread of the beam, and the central energy was taken half-way between them. The final beam energies were determined from the range curves to be 313±14 MeV and 371±13 MeV.

3. Beam Contamination

The beam contamination consists of muons and electrons. Some of the pion decays, $\pi^- \rightarrow \mu^- + \bar{\nu}$, occur before the analyzing magnet, and the resulting muons that pass through this magnet and remain in the beam have only the momentum of the main pion beam. These are observed in the range curve at point B after the electron-component curve is extended back to this point from point C, and subtracted. However other pion decays occur after the bending magnet, and the muons produced there occur with a spectrum of momenta. The number of these

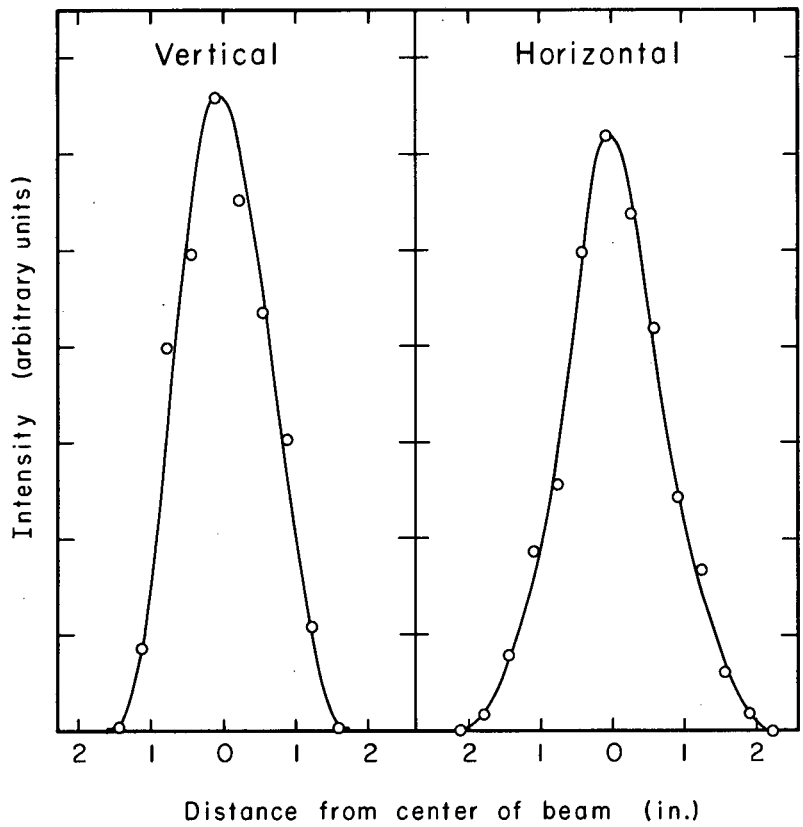

Fig. 3. Vertical and horizontal profiles of the 371-MeV beam taken at the position of the liquid hydrogen target.

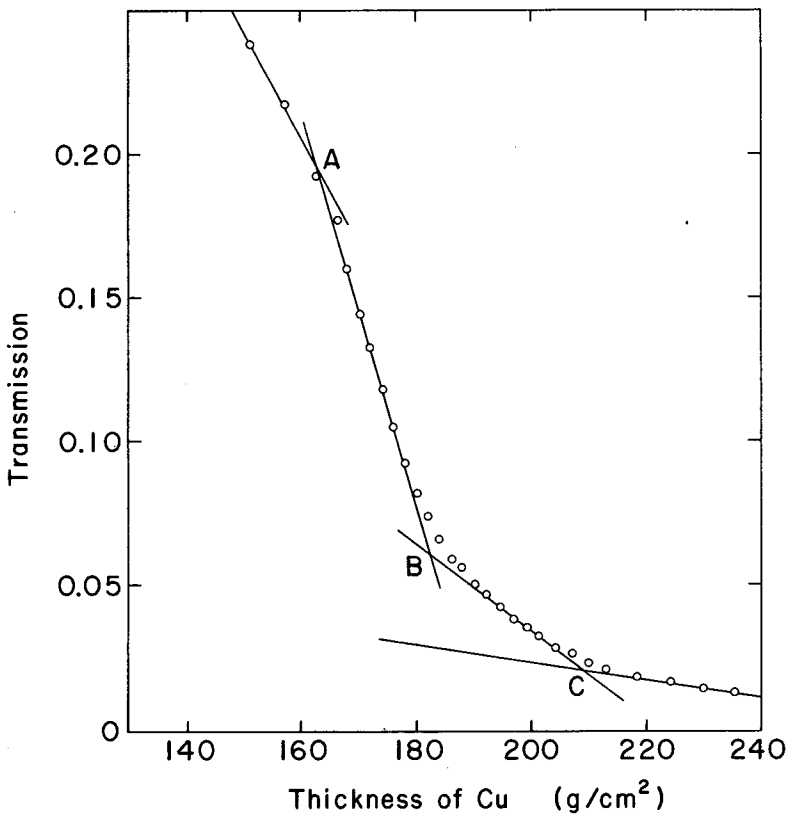

Fig. 4. Integral-range curve for 313-MeV π^- beam.

muons can be calculated and added to the others already accounted for. However the range distribution of this second group must also be computed, since the muons of this group with a range greater than that corresponding to point B have already been counted in the range curve and must not be recorded twice. With this precaution observed, we have obtained the fraction of the muon contamination of the beam shown in Table I.

Table I. Summary of π^- beam characteristics.

Energy (MeV)	ΔT (MeV)	Intensity (π/min)	Muon contamination (%)	Electron contamination (%)
313	14	25×10^6	5.8	0.3
371	13	12×10^6	4.0	0.3

Beyond point C in the range curve the multiply scattered electrons that appear do not faithfully represent the number of electrons traversing the system under operating conditions, since many of them arise from electron showers in the copper absorber. Therefore the electron contamination was estimated to be 0.3% from measurements made on almost identical beams with gas Čerenkov counters.[18] The properties of the beam are summarized in Table I.

B. Liquid Hydrogen Target

The liquid hydrogen target was located at the final focus of the beam system after the beam had passed through an aperture in a 4-ft. concrete shielding wall. The target was a modified version of one used successfully before.[10] The hydrogen target is shown in Fig. 5. This target could accommodate the cylindrical scintillation counter (S_4) used to separate final neutron states associated with charged pions. It also had a minimum amount of material surrounding the hydrogen flask, which could rescatter the neutrons or act as converter for the gamma

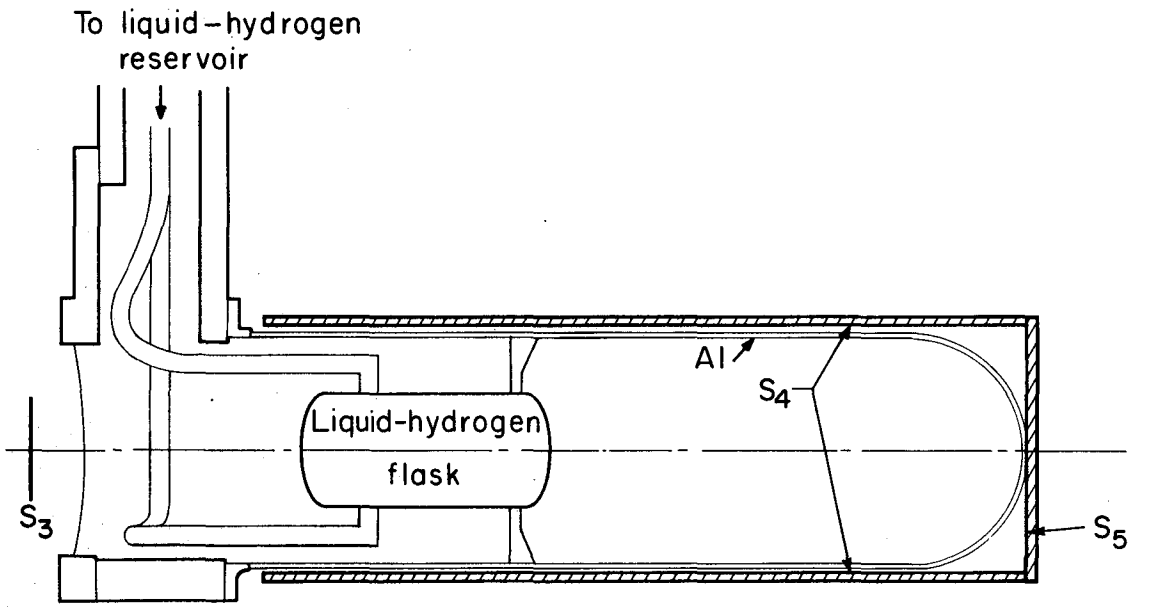

Fig. 5. Liquid hydrogen target showing the last of the three beam-monitor counters and the surrounding scintillation counters.

rays leaving the target. The vacuum chamber consisted of a 6-in.-diameter aluminum cylinder with 0.04-in. walls and a 0.02-in. spun-aluminum end dome. The front window of the vacuum chamber consisted of Mylar 0.03-in. thick.

The liquid hydrogen flask was a horizontal cylinder 3-in. in diameter and 6-in. long with walls of 0.015-in. Mylar. The ends were also formed of 0.015-in. Mylar. The flask was supported in the vacuum chamber by Styrofoam braces. Because the ends of the flask were slightly curved, the mean value of the target length was obtained by averaging the physical flask length weighted by the beam profile over the cross-sectional area of the flask. This value was 5.73 in. for the 313-MeV beam and 5.76 in. for the 371-MeV beam. The slight difference is due, of course, to slightly different beam profiles. These values were used later as the effective target length in calculating the differential cross sections from the observed neutron yields.

C. Scintillation Counters

Figure 6 shows the arrangement of the experimental area. Located along the pion beam are four scintillation counters (S_1, S_2, S_3, and S_5), which form the beam-monitoring system. Surrounding the hydrogen target is the counter (S_4) used to detect charged pions. The relative positions of S_3, S_4, S_5 and the target are also shown in greater detail in Fig. 5. The four neutron counters (N_{1-4} surrounded by anti-coincidence counters A_{1-4}) are located at representative positions for detecting neutral particles originating in the target.

1. Beam-Monitor System

Counters S_1, S_2, and S_3 were located in the beam to monitor the incident-pion flux arriving at the target position. The smallest counter S_3 defined the area of the beam accepted by the monitor system. This counter was made as thin as practical (1/16 in.) so as to reduce the number of non-hydrogen-scattered particles accepted by the system. Therefore the zero-time signal for the time-of-flight analysis was not derived from this counter because the timing resolution would have

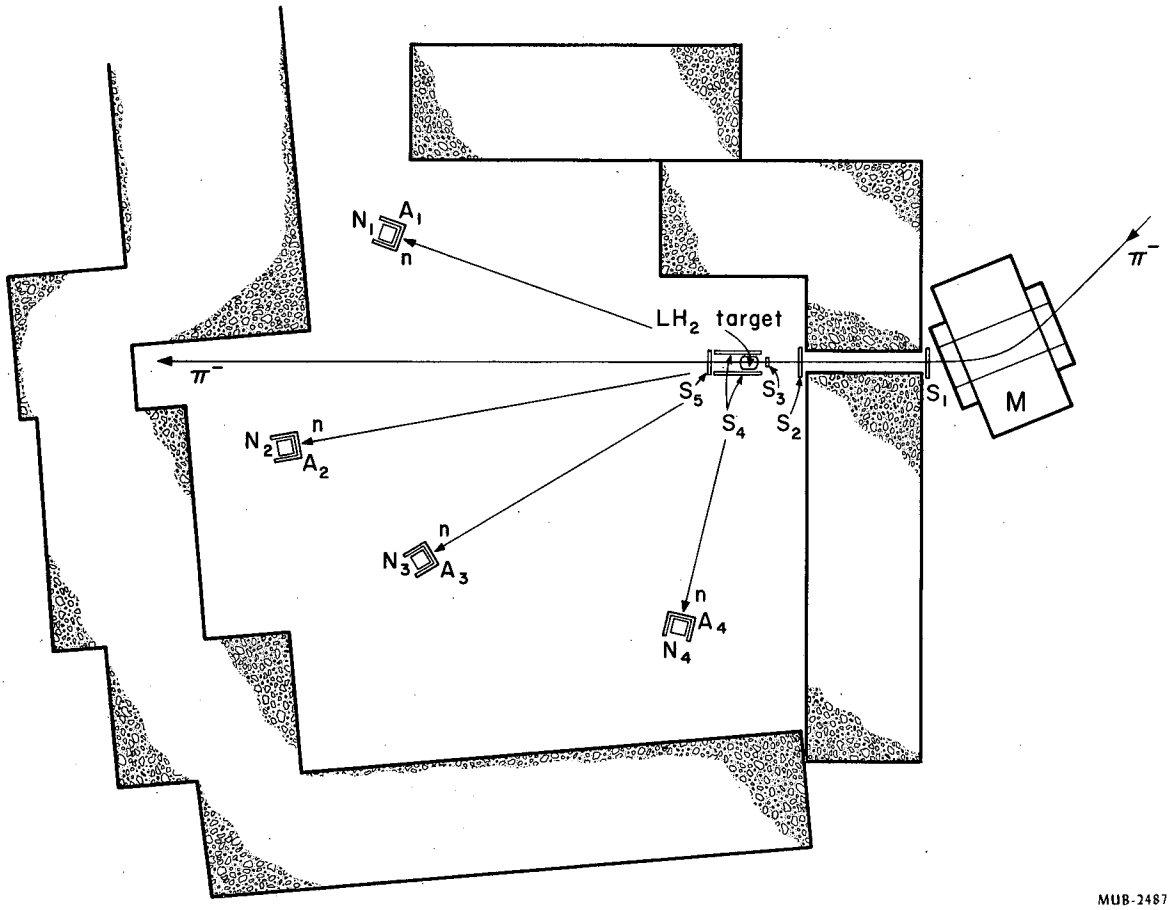

Fig. 6. Plan view of the experimental area showing target and counter arrangement.

been adversely affected by the statistical fluctuations in the small number of photoelectrons produced at the photocathode by a particle passing through this thin scintillator. Instead, S_2 served as the source of the zero-time signal, since it could safely be made somewhat thicker. Counter S_5, located beyond the hydrogen target and used in anticoincidence, rejected incident pions that were not scattered by an angle greater than 10 deg in the hydrogen. This eliminated false start-time signals from noninteracting particles, and reduced the start-time signal rate by a factor of almost 25.

Each of these counters was made from a circular disk of plastic scintillator optically connected by a Lucite light pipe to a photomultiplier tube. Their dimensions and phototube types are listed in Table II. The RCA 7264 phototube was selected for the zero-time counter for its better timing characteristics.[19]

Table II. Counter description.

Counter	Dimensions		Phototube type
	Thickness (in.)	Diameter (in.)	
S_1	1/4	7	RCA 6810A
S_2	1/4	5	RCA 7264
S_3	1/16	2 1/2	RCA 6810A
S_5	1/2	7	RCA 6810A

2. Charged-Pion Counter

Counter S_4 surrounded the liquid hydrogen target and detected the presence of one or both of the charged pions in coincidence with a neutron from reaction (5). Thus these "charged mode" neutron events could be recorded separately from the "neutral mode" events [reactions (2) or (4)]. This scintillation counter was in the form of a horizontal cylinder with an outside diameter of 7 in., a length of 20 in., and a wall thickness of 1/4 in. It was viewed by two RCA 6810A phototubes optically connected to it by Lucite light pipes. The two phototube-output pulses were added to form the S_4 signal.

3. Neutron Counters

Neutrons were detected in a block of plastic scintillator by the light produced by recoiling charged products arising in interactions between the incident neutrons and the hydrogen or carbon nuclei of the scintillator. Gamma rays were similarly registered by the counter, but these could be clearly distinguished by their earlier arrival time.

Figure 7 shows one of the four identical neutron counters prior to assembly. The scintillator block was 4-in. thick in the direction of neutron penetration, and had an octagonal frontal area formed by removing the corners of a 4×10-in. rectangle. Thus the area intercepting neutrons was 38 in.^{2} and the scintillating volume was 152 in.^{3} One face of the detector was attached directly to a Lucite light pipe, which in turn was optically connected directly to the photocathode of the phototube. All other sides of the scintillator block were covered with a white plastic paint (Tygon series K) to provide a diffuse reflective surface that improved the light collection slightly.

A phototube with a photocathode 5-1/4 in. in diameter was used in order to obtain efficient light collection from the large block of scintillator. The phototube (Amperex 58AVP) was selected because it had the best timing characteristics of the tubes with a large photocathode. The pulse rise time was slightly better, and the cathode transit-time differences considerably better, than with any other phototube available.

Each anticoincidence counter was an octagonal box completely surrounding the scintillator block and extending back an additional 4 in. beyond the sensitive area. The front face and sides of this counter were formed of 1/4-in. plastic scintillator, and were viewed through Lucite light pipes by two RCA 6810A phototubes whose signals were added. The efficiency of the counter was estimated at $> 99.5\%$.

Figure 8 shows a neutron detector assembled and mounted in its movable frame. The four neutron counters recorded data simultaneously, from positions on both sides of the π^- beam, and at laboratory angles from 10 to 60 deg. It was not practical to take data at smaller angles because of the close proximity of the noninteracting π^- beam,

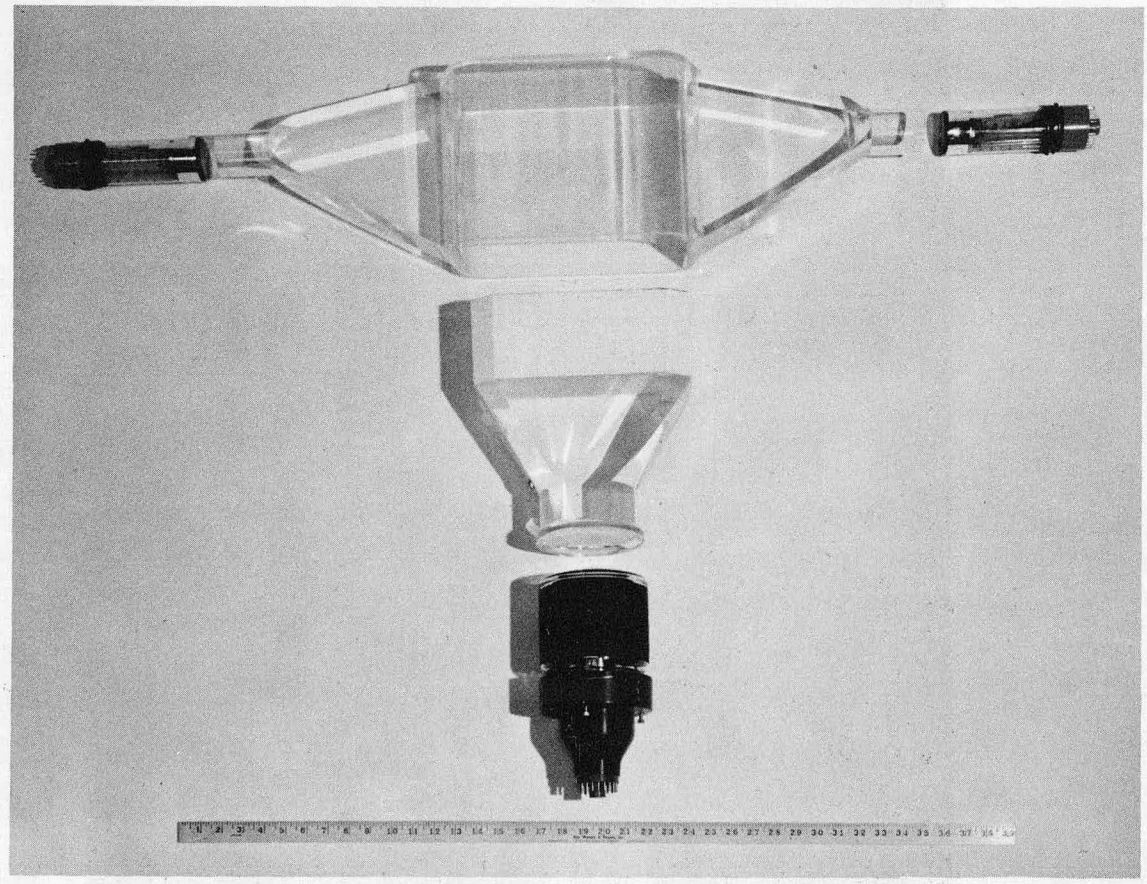

ZN-4343

Fig. 7. Unassembled neutron counter showing the anti-coincidence counter with its two phototubes, the scintillator block attached to the light pipe, and the neutron phototube.

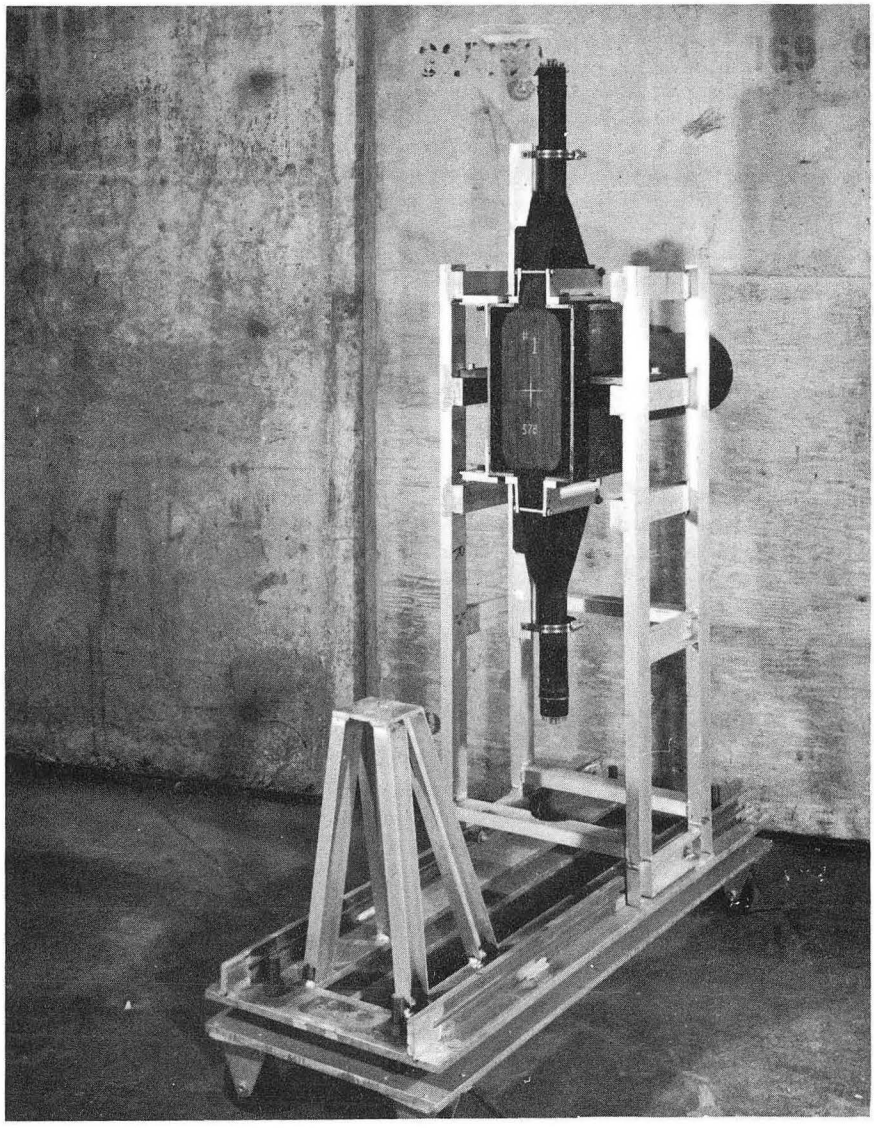

ZN-4342

Fig. 8. Assembled neutron counter.

nor at large angles because at these angles the neutrons were of such low energy that the neutron-detection efficiency of the counters was not adequately known.

D. Electronics

Sufficient information was now contained in the signals from the various particle detectors to separate the neutrons being observed from reactions (2), (4), and (5). This separation and the proper tabulation of these various events was performed by the electronics system. A simplified schematic diagram of this system is shown in Fig. 9. Only essential electronic functions are represented and many circuits are omitted for clarity. Also, only one of the four neutron detectors is shown. We describe in somewhat greater detail the components and operation of this system. References to special circuits are by LRL Engineering Drawing number. Descriptions of all other circuits are given in the LRL Counting Handbook.[19]

1. Beam Monitoring

The phototube pulses from all the counters in the electronic system triggered tunnel-diode discriminators whose outputs were uniform in amplitude and time duration. This triggering was beneficial since it provided uniform pulses at the coincidence circuits. The monitor coincidence circuit "M" used such pulses from S_1, S_2, and S_3 to form a 123 coincidence, which signalled the passage of an incident pion in the beam. Likewise a $123\overline{5}$ response ($\overline{\ }$ denotes anticoincidence) in circuit "I" indicated that a pion had interacted in the target.

Account had to be taken at this point of the fact that the cyclotron beam was produced in 15-nsec bunches with a frequency of one bunch per 54 nsec. The monitor counters could not resolve two pions in the same bunch. In such cases one pion might interact and have the resulting neutron properly detected, but then have the event rejected because the other pion tripped anticoincidence counter 5. Since the probability of two pions' occurring in the same bunch is equal to the probability of two pions' occurring in bunches separated by 108 nsec,

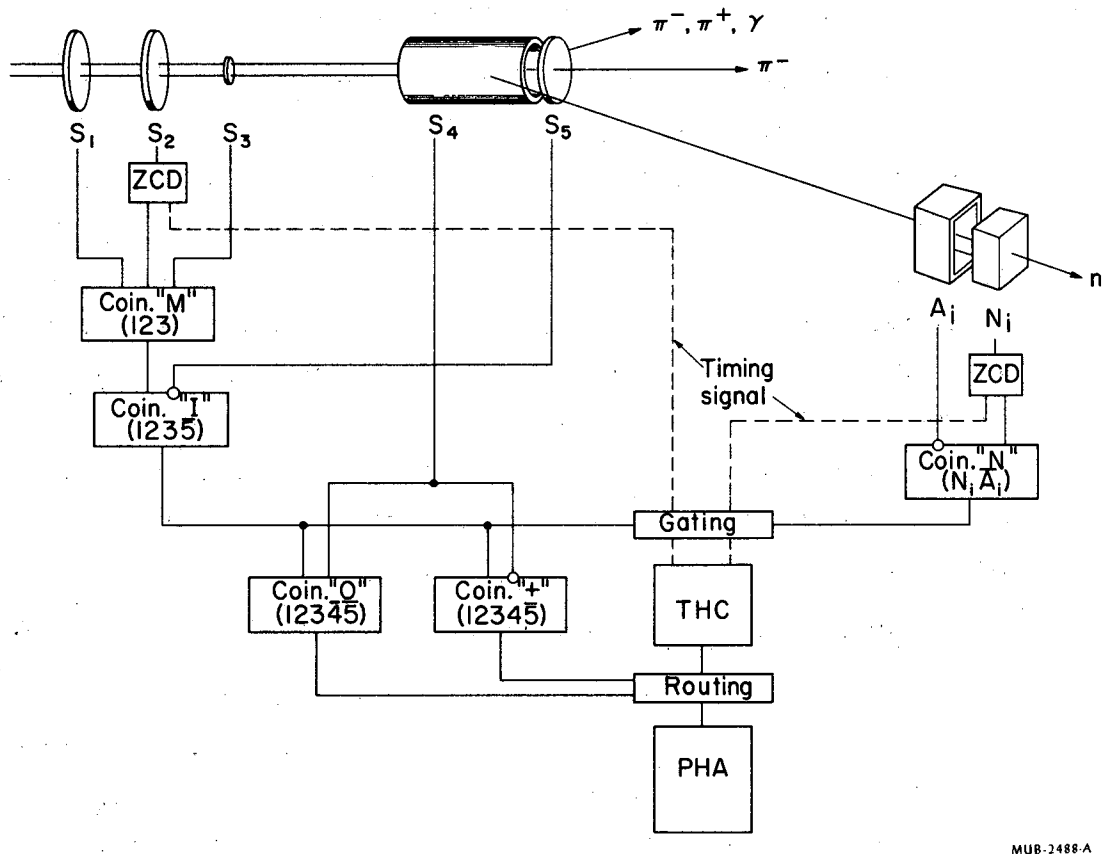

Fig. 9. Simplified electronic block diagram. Four neutron detectors (N_i and A_i) were used in the experiment.

ZCD = zero crossing discriminator
THC = time-to-height converter
PHA = pulse-height analyzer

the beam-monitor counting rate was properly compensated by placing a signal from S_5 in anticoincidence in the "M" circuit after being delayed by 108 nsec. This reduced the monitor counts by the number of pions that might interact and then be improperly rejected.

The auxiliary-dee facility of the 184-inch cyclotron was used throughout this experiment. This mode of operation spilled the internal proton beam onto the Be target over a period of 6 to 10 msec instead of the normal maximum duration of 400 μsec. However, even with this "stretched" beam, 10 to 20% of the pion flux was located in the first 200 μsec of the spill and resulted in an unacceptably high instantaneous intensity. The electronic system was therefore gated off during this so-called "spike." All scalers in the system were controlled by this gate signal. In addition the system was gated off during the time that the pulse-height analyzer (PHA) was busy. However this dead time amounted to less than 0.1%. The beam monitor 20-Mc discriminator-scaler system was doubled for reliability.

2. Neutron Time-of-Flight Analysis

Besides the signal supplied to the beam-monitor circuits, S_2 also provided the zero-time or "start" signal for the time-to-height converter (THC) of the time-of-flight system. This signal was in the form of a clipping-line-differentiated pulse at the input to the tunnel-diode discriminator (5X-2192-4).

The "stop" signal was generated when a neutral particle registered in one of the neutron detectors N_{1-4}. This neutron-timing information was obtained from the phototube (58AVP) signal by pulse differentiation with an overdamped LC-tuned circuit to produce a zero-crossing signal whose zero-crossing point was detected by a tunnel-diode discriminator (5X-2193-3). This technique was used because the time shift of the output pulse is very small over a large dynamic range of photomultiplier-input light levels.[20]

In order to prevent pulse saturation that would spoil the timing information of the differentiated pulse, the phototube base was a graded-voltage-divider chain. Two signals were taken from the neutron tube

base. In addition to the anode pulse used for timing information, a normal signal was taken from dynode 14 and its amplitude information was used to set the threshold of the tunnel-diode discriminator.

This discriminator, in turn, generated two pulses. The one containing the accurate timing information was the "stop" signal for the THC. The other went to the appropriate neutron coincidence circuit N. The A_{1-4} signals, placed in anticoincidence at these four circuits, rejected pulses arising from initially charged particles entering the neutron counters.

The summed output of the four N coincidence circuits controlled one element of the gating circuit (4X-1112-6D). When one of the neutron counters detected a neutral particle within 90 nsec after a $123\overline{5}$ coincidence had indicated that a pion had interacted in the target, the I signal passed through this first gate to open a second set of gates, which allowed the timing signals--the "start" and "stop" pulses--to enter the THC. This THC unit consisted of two tunnel-diode discriminators (4X-1112-18) to shape the pulses--the actual time-to-height converter (4X-6422A), and a linear amplifier (LRL Model V). The THC provided a signal whose amplitude was proportional to the separation between the time of the start and stop pulses--that is, proportional to the time between the pion interaction and the arrival of the neutral particle at the neutron counter.

3. Signal Routing

The signals from the THC contained data from both "charged and neutral mode" events, which were recorded by all of the neutron counters positioned at different laboratory angles and flight-path distances from the target. Each type of event and experimental condition had to be sorted, identified, and recorded separately. This was done by the routing matrix.

The presence or absence of an S_4 signal accompanying an interacting pion distinguished a charged from a neutral mode neutron event. Thus a $1234\overline{5}$ response in the "+" coincidence circuit indicated an interacting incident pion with charged reaction products, whereas a

$12\overline{345}$ signal out of the "0" circuit indicated a reaction with all neutral products. The outputs of the discriminators following these coincidence circuits were the inputs to two routing-pulse generators (5X-2652). The other inputs came from the N coincidence units and indicated which neutron counter had provided the detection signal. The output signals from these generators were of the proper polarity and duration to supply the external routing inputs to two 400-channel RIDL pulse-height analyzers (PHA). The analyzers were used in the external-routing four-quadrant mode of operation, for which the first unit recorded all neutral-mode events and the second handled the charged-mode events. The channels of both units were numbered and read-out sequentially. Thus the data stored in locations 000-099 corresponded to neutral events detected by neutron counter N_1. Likewise locations 500-599 contained charged data from N_2.

An OR circuit (4X-6381-17) in the routing matrix prevented ambiguous combinations of routing and signal inputs from reaching the PHA. Each input signal analyzed was accompanied by one and only one routing pulse. The frequency with which signals arrived for analysis at the PHA was low enough to exclude any problems involving loss of efficiency due to this circuit.

At appropriate time intervals the contents of the magnetic-core memory units of the PHA were read-out on punched paper tape and printed on an IBM typewriter. Included with the data was a coded numerical "title" that uniquely specified the particular run and recorded the appropriate experimental conditions of the beam, target, and each of the four neutron counters.

E. Experimental Procedures

Since some detected events occurred in the material of the target flask and vacuum jacket rather than in the liquid hydrogen itself, these events were accounted for by taking data with the target full of hydrogen and again with it empty. The difference between the two sets of data represents the events taking place exclusively in the hydrogen.

However for both target configurations, random accidental coincidences occurred at a definitely nonnegligible rate. These accidental rates were measured by inserting 108 nsec of delay in the start side of the time-of-flight system, including routing. This put the entire system out of coincidence by two fine-structure cyclotron pulses. Again by subtracting the corresponding sets of data, channel by channel, information free from the most prevalent form of electronic accidentals was obtained.

The measurements were performed in cycles of target-full-real target-full-accidental, target-empty-acidental, and target-empty-real. In order to minimize the statistical error in the data for the available running time, the relative time spent on each type of measurement was proportional to the square root of the counting rate for that condition.

Since the time separation between the arrival of the elastic and inelastic neutrons varied considerably with angle, it was desirable to use various flight-path lengths. At the most forward angle (10 deg), where the velocities of the two types of neutrons was most nearly equal, it was necessary to use a flight path of 5 meters to obtain a clear separation between the elastic and inelastic events recorded in the PHA. However, at large laboratory angles, adequate separation could be obtained at 3 meters. Therefore we decreased the path length at these angles to take advantage of the higher counting rates achieved from the larger solid angles subtended by the neutron detectors. At intermediate angles, 4 meters was a useful compromise. At some angles, data were taken for two different path lengths.

Data were also taken with two different detection thresholds for the neutron counters. Since neutrons could give rise to arbitrarily small light signals in the blocks of plastic scintillator, some minimum acceptable light level had to be established. Since the neutron-detection efficiency is a sensitive function of what minimum level is selected, this had to be rechecked periodically throughout the experiment. This threshold was set with the Compton edge of the 1.28-MeV γ ray from Na^{22}. The energy distribution of the Compton electrons produced by this γ ray has a sharp maximum at 1.07 MeV. The threshold for

detection was controlled by the discriminator triggered by the dynode signal from the 58AVP phototube. The dynode signal was split and stretched for input into the PHA. The pulse-height spectrum of a Na^{22} source placed against the neutron detector was displayed and the threshold of the dynode discriminator set at the location of the Compton edge (see Fig. 10). Attenuators were then used in front of this discriminator to set the thresholds at levels higher than 1.07 MeV. Data were taken at thresholds of 2.09- and 8.31-MeV equivalent electron energy.

A summary of the experimental running conditions is given in Table III.

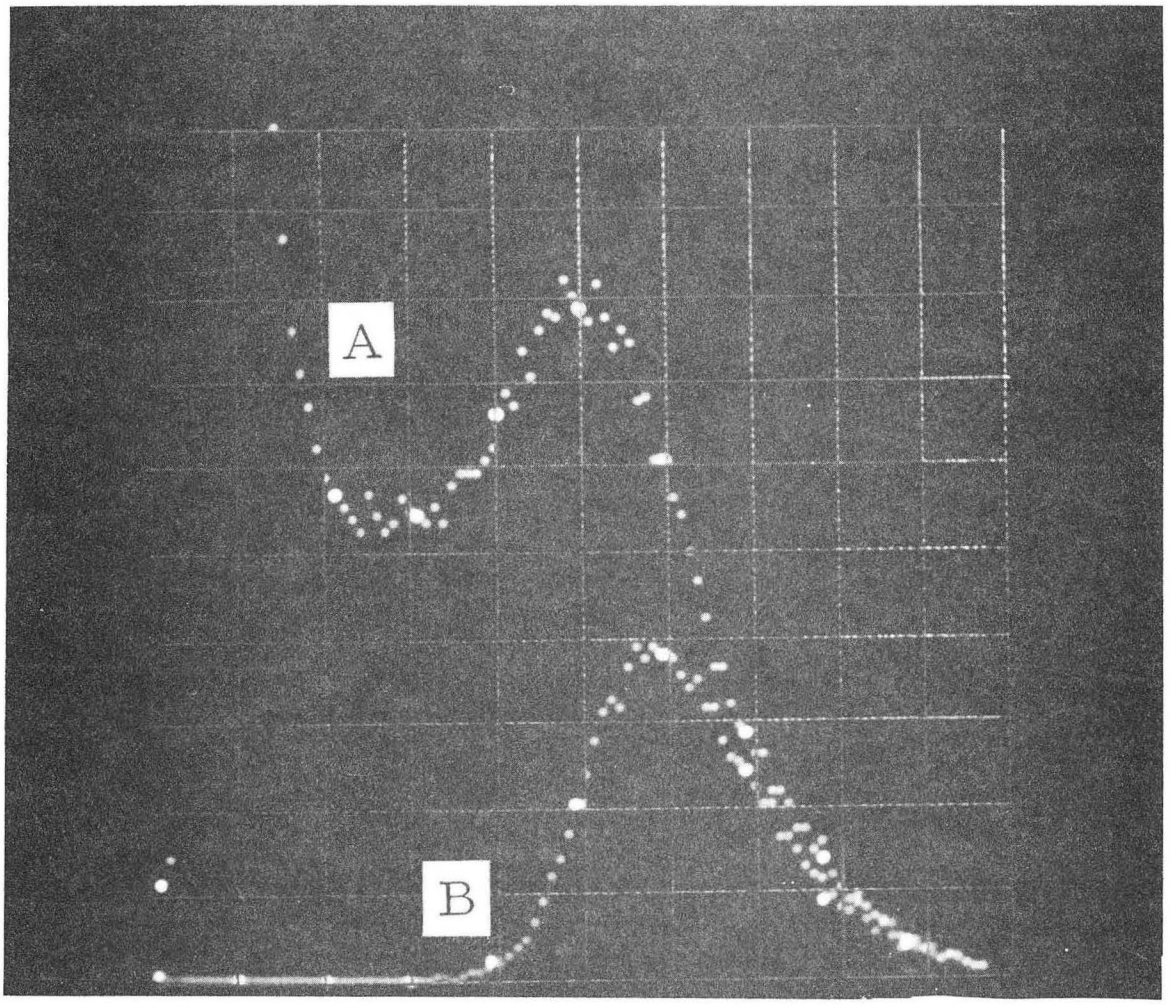

ZN-4344

Fig. 10. Compton edge of Na^{22} observed by neutron detectors. A. Measured spectrum of Compton electrons produced by 1.28-MeV γ from Na^{22} source. B. Measured spectrum with cut-off by amplitude discriminator.

Table III. Summary of experimental running conditions.

π^- Beam energy (MeV)	Neutron angle (deg)	Flight path (meters)	Detection threshold	
313	10	5	8.31	
		4	8.31	2.09
	15	4	8.31	2.09
	20	4	8.31	
		3	8.31	
	25	4	8.31	
		3	8.31	2.09
	30	3	8.31	
	40	3	8.31	2.09
	45	3	8.31	
	50	3	8.31	
	55	3	8.31	
	60	3	8.31	2.09
371	10	5	8.31	
	20	4	8.31	
	30	3	8.31	
	40	3	8.31	
	50	3	8.31	
	60	3	8.31	

III. DATA ANALYSIS

After the necessary data had been accumulated, the cyclotron facilities were relinquished to other experimenters, and our experiment proceeded into the data-analysis stage. First, the data that had been recorded on punched paper tape were transferred to magnetic tape. In the process, checks were made for clerical errors and consistency between runs. Second, the yield per incident pion per PHA channel was computed. Then all the data from the various runs for each set of experimental conditions were combined. At this point, several normalizing corrections were applied to these combined yields. Finally we computed the differential cross section $d\sigma/d\Omega$ for the elastic neutrons and the double-differential cross section at constant neutron lab kinetic energy $d^2\sigma/dT\, d\Omega$ for the inelastic neutrons.

Let us now look more carefully at the steps of the data analysis.

A. Yield

From the data taken with the hydrogen target alternately full and empty, and with the electronics timed for first real and then accidental events, we computed the yield per incident pion per PHA channel for hydrogen Y_i, and its statistical error ΔY_i. The data from each of the eight sections of the PHA memory were separately combined, channel by channel, for each cycle of runs according to

$$Y_i = \left(\frac{F_i}{M_F} - \frac{FA_i}{M_{FA}}\right) - \left(\frac{E_i}{M_E} - \frac{EA_i}{M_{EA}}\right)$$

$$\Delta Y_i = \left(\frac{F_i}{M_F^2} + \frac{FA_i}{M_{FA}^2} + \frac{E_i}{M_E^2} + \frac{EA_i}{M_{EA}^2}\right)^{1/2},$$

where

F_i = number of neutral real counts in channel i during a run with the hydrogen target full, and

M_F = number of incident particles detected by the monitor system during this same run.

The remaining symbols represent the corresponding quantities, where E, FA, EA indicate the experimental conditions, respectively, of hydrogen target empty and electronics normal; target full, electronics accidental; and target empty, electronics accidental.

Figure 11 illustrates this yield after all runs for a particular experimental condition had been combined. The yield is shown as a function of PHA channel number which is proportional to the time of flight from the target to the detector. The first particles to arrive are the γ rays, which form the large peak centered at channel 27. These are clearly distinguishable from the elastic neutrons that arrived next and formed the peak at channel 50. Finally the slower inelastic neutrons are distributed over the next 30 or so channels. Figure 11 was chosen to illustrate the worst situation we encountered, as far as separating the elastic from the inelastic neutrons was concerned. At 313 MeV, the lower π^- energy, the reduced inelastic cross section left the elastic peak much more clearly defined. Also at this particular laboratory angle of 20 deg, the flight-path distance and statistical fluctuations due to the low yield combine to leave the least distinguishable "valley" between the two types of neutrons. Still, at this most adverse condition, we were able to unambiguously fit the elastic-neutron peak with a Gaussian curve whose area represents the total-elastic-neutron yield at this angle.

The over-all timing resolution for the entire system is easily seen in the gamma peak. With perfect resolution this peak would be a delta function and would appear in a single PHA channel. Thus any broadening of the gamma peak directly represents the resolution function of the electronic system, since fluctuations in the flight path due to the finite size of the target and the detector are negligibly small. The timing resolution of our system was quite adequate to separate the inelastic neutrons, since the full-widths at half-maximum of the gamma peaks were all near 1.5 nsec.

An interesting but at first disconcerting effect is represented by the small peak at channel 15. At first glance this appears to be a neutral particle arriving at the detector some 6 nsec before the gamma

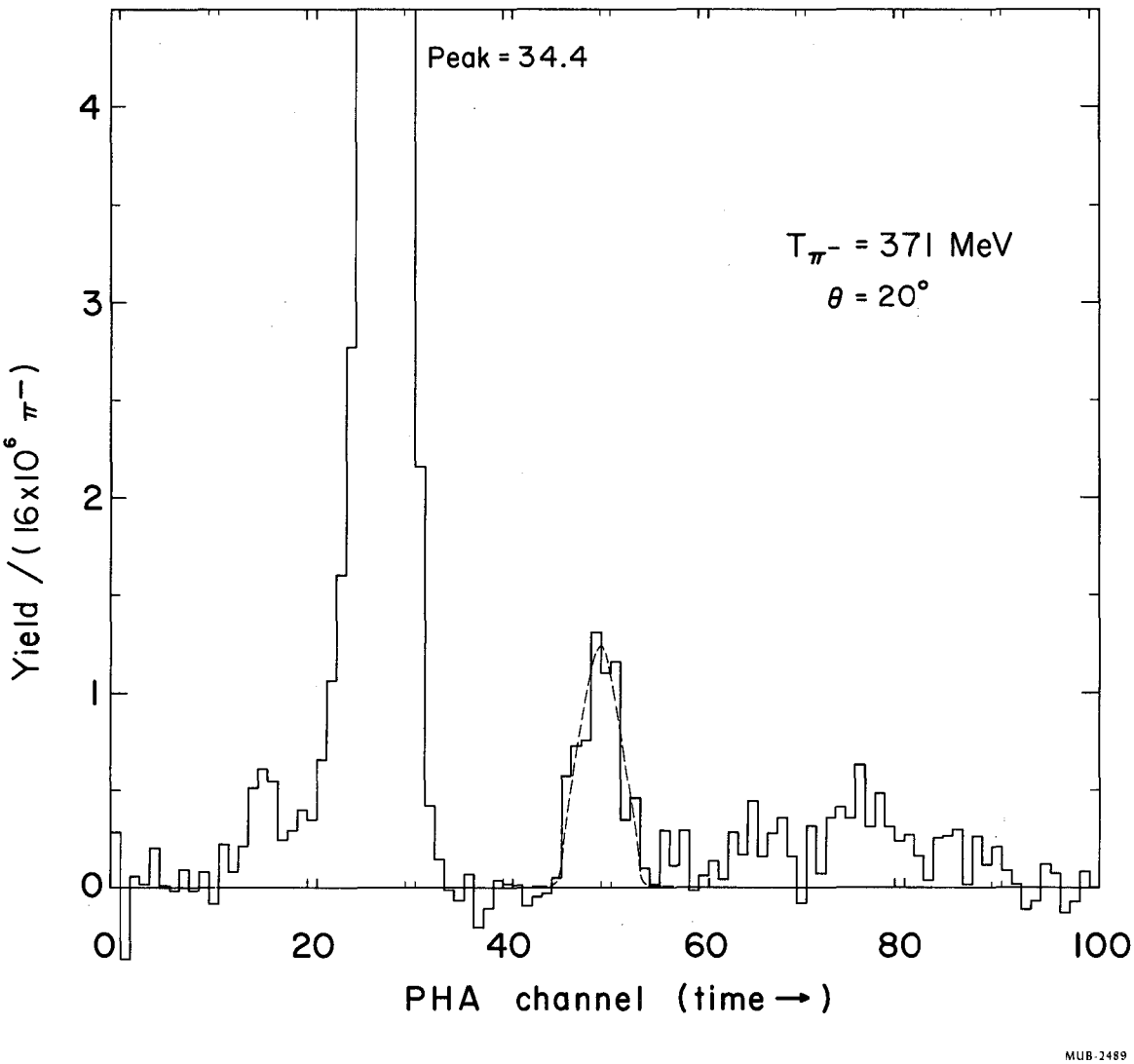

Fig. 11. Neutral-mode time-of-flight spectra. The solid line histogram is the neutral-particle yield. The dashed line is a Gaussian curve fitted to the elastic-neutron peak. (The detailed structure of the spectra is discussed in the text.)

rays arrived. This of course would require a velocity somewhat greater than the speed of light! Further investigation, however, revealed that it was due to a much less spectacular effect.

The zero-crossing timing technique is pulse-shape-sensitive in that the timing signal shifts slightly if the centroid of the area under the signal moves when two differently shaped signals are received.[20] Investigation showed that the Čerenkov radiation produced in the Lucite light pipe by some γ-ray-produced electrons generated a pulse in the neutron detector that was much more symmetrical than the rapidly rising but slowly decaying pulse from the neutrons. The resulting shift in the stop signal to the THC caused a fraction of the gamma rays to register about 12 channels too low in the PHA. Since this effect could not arise from the much slower neutrons, which were our real concern, it could be handled in either of two ways. Since the Čerenkov light levels were small, the spurious peak could be eliminated by raising the detection threshold, or by simply ignoring it. We used both techniques.

B. Corrections

Before the differential cross sections that constitute the results of this experiment could be calculated from the neutron yields that we had so far obtained, it was necessary to normalize these yields by the following series of corrections.

1. Neutron-Detection Efficiency

The neutron-detection efficiency of plastic scintillator (CH) is a function of neutron energy, the threshold for the detection of scintillation light, and the detector geometry. At the neutron energies encountered in this experiment, scintillation light is produced not only from the charged products of the neutron-proton (n-p) interactions, but also from neutron-carbon (n-C) reactions with charged final-state products, such as C(n,α)Be, C(n,n'3α), C(n,p)B, or C(n,np)B. Also since the dimensions of the detectors are of the same order of magnitude as the mean-free path for neutron interactions, the rescattering of the final-state neutrons also contributes to the efficiency.

An IBM 709-7090 FORTRAN program called TOTEFF[21] was used to compute the neutron-detection efficiency ϵ as a function of neutron energy E for each of the two detection thresholds, T at which data were taken. The efficiency is computed from the folding integration

$$\epsilon(E) = \int_0^\infty dT \exp\left\{ - \left[(T - T_0)/\tau T_0 \right]^2 \right\} \epsilon(E, T),$$

where T_0 is the mean threshold, τ is the fraction resolution, and $\epsilon(E, T)$ is the efficiency at energy E and threshold T. The term $\epsilon(E, T)$ contains contributions from the interactions with both hydrogen and carbon nuclei. Reference 21 describes the calculation in considerable detail. Figure 12 shows the variation of the efficiency with neutron energy and detection threshold as derived from this calculation. The uncertainty estimated for the efficiency is ± 10% and is regarded as an upper limit. We were confident of the calculation since the efficiency values obtained from this program are compatible with corresponding measurements made by Wiegand et al.[22]

2. Gamma Conversion

Neutral pion mesons occur as final-state particles in both elastic- and neutral-mode inelastic interactions. As the γ rays into which these mesons decay pass through the material of the target and surrounding counters, there is a finite probability of one or more of the γ ray's producing an e^+, e^- pair. If this happens, or if the neutral pion decays in the $\pi^0 \rightarrow \gamma + e^- + e^+$ mode and one of the charged particles passes through scintillation counter S_5, the event would be lost. This turns out to be a negligible effect. However if one of the charged particles is detected by S_4, the accompanying neutron would be misconstrued as having arisen from the $\pi^- + p \rightarrow \pi^+ + \pi^- + n$ interaction and the event would be routed to the charged-mode section of the PHA. Therefore the probability for gamma conversion as a function of the laboratory angular distribution of the final neutral particles must be

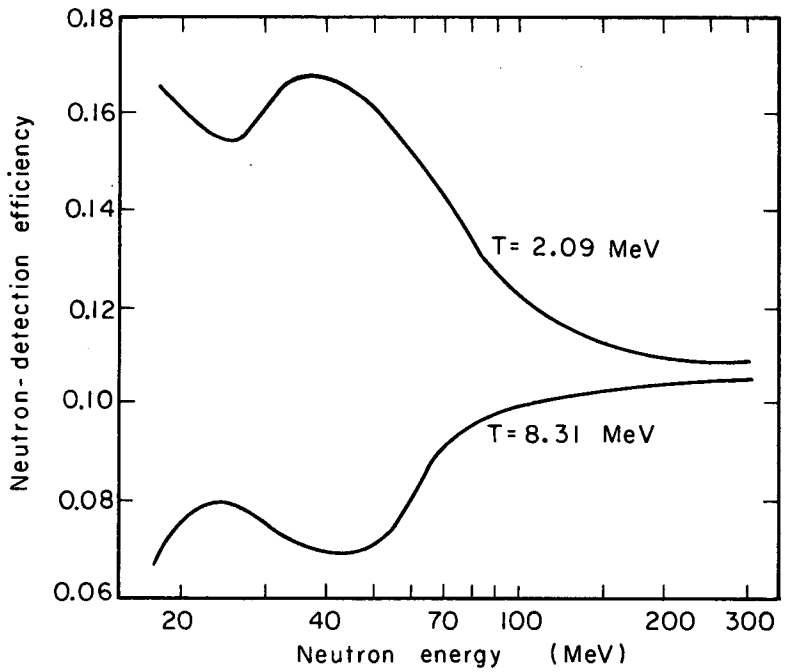

Fig. 12. Neutron-detection efficiency for a counter 10.16 cm thick with a fractional resolution τ of 0.15 and at detection thresholds T of 2.09 and 8.31 MeV.

calculated so that misrouted events can be analytically transferred from the charged- to the neutral-mode data.

The calculation of the gamma conversion is described in Appendix A. Figure 13 shows the total probability that either of the two π^0-decay γ rays associated with an elastic neutron will convert and register in the S_4 counter, plotted as a function of the laboratory angle of the associated neutron. The probability that any one of the four gammas (two π^0's) associated with an inelastic neutron would convert is twice this value. For both types of neutrons, if the appropriate conversion probability is called P_γ, then the enhancement to the neutral mode yield is $1/1-P_\gamma$. At the same time an equal number of events must be removed from the charged-mode yield.

3. Neutron Rescattering and Absorption

After the initial scattering process in which they are produced, the neutrons can interact with nuclei in the material immediately surrounding the target. This can be either by elastic rescattering, in which case no neutrons would be lost, but the differential distribution of the neutrons might be altered; or the neutrons could interact inelastically with the target nuclei and be absorbed, decreasing the apparent flux at the neutron detectors.

Measurements and calculations of the effect of rescattering on the distribution of elastic neutrons had been made by Kurz at 374 MeV.[10] When neutron rescattering was increased by surrounding the target with 1/8 in. of copper and an additional S_4 counter, no statistically significant change in the distribution was observed. This agreed with initial estimates made by computing the total rescattering cross section,

$$\sigma_T^r = \int d\Omega_1 \; \frac{d\sigma_1}{d\Omega}(\theta_1)\, nt(\theta_1)\, \sigma_2^T [T_1(\theta_1)],$$

where $d\sigma_1/d\Omega$ is the differential cross section for the original scattering process at angle θ_1; nt is the number of scatterers per cm^2 for the rescattering reaction; and $\sigma_2 T$ is the total cross section for the rescattering reaction at incident energy T_1.

The qualitative behavior of rescattering is to shift the elastic-neutron distribution toward the smaller angles where the cross section is lowest. At 313 MeV, even the most adverse assumptions indicated that such a shift would be less than the uncertainty of the neutron-detection-efficiency calculation. Therefore no correction was applied to the data at either energy for elastic-neutron rescattering. Likewise, even with the rising value of σ_{np} that dominates the rescattering at the lower average energies of the inelastic neutrons, a shift in the distribution would be insignificant compared with the statistical uncertainty of the inelastic-neutron data.

In addition to the elastic-rescattering processes, neutrons are absorbed in the inelastic reactions with target nuclei. In reactions such as $C^{12}(n, \alpha)Be^{9}$ and $Al^{27}(n, p)Mg^{27}$, no neutrons exist in the final state. Appendix B describes the calculation of the decrease in the neutron flux due to these inelastic processes. This attenuation varies as a function or neutron laboratory angle (as shown in Fig. 13) due to the changes in neutron energy, as well as the varying amount of material encountered when the neutron leaves the target in various directions. If the fraction of unabsorbed neutrons is f_n, the neutron yield must be corrected by the factor $1/f_n$.

4. Beam-Monitor Corrections

Neutron yields are obtained by normalizing the counting rates of the neutron detectors by the incident flux of negative pions on the target, as measured by the beam-monitoring system. However, as indicated in Table I, the 313- and 371-MeV beams contained, respectively, 6.1% and 4.3% contaminations of muons and electrons. Since these particles do not interact strongly with the target protons, the beam-monitor counting rate was corrected to correspond to the fraction of pions in the beam. This was done by multiplying the yields by the factor $1/1\text{-}C_{\mu e}$, where $C_{\mu e}$ is the combined fractional contamination.

5. Beam-Profile Corrections

Slight corrections were made to the data to reflect the shape of the beam profiles shown in Fig. 3. This was necessary for two reasons.

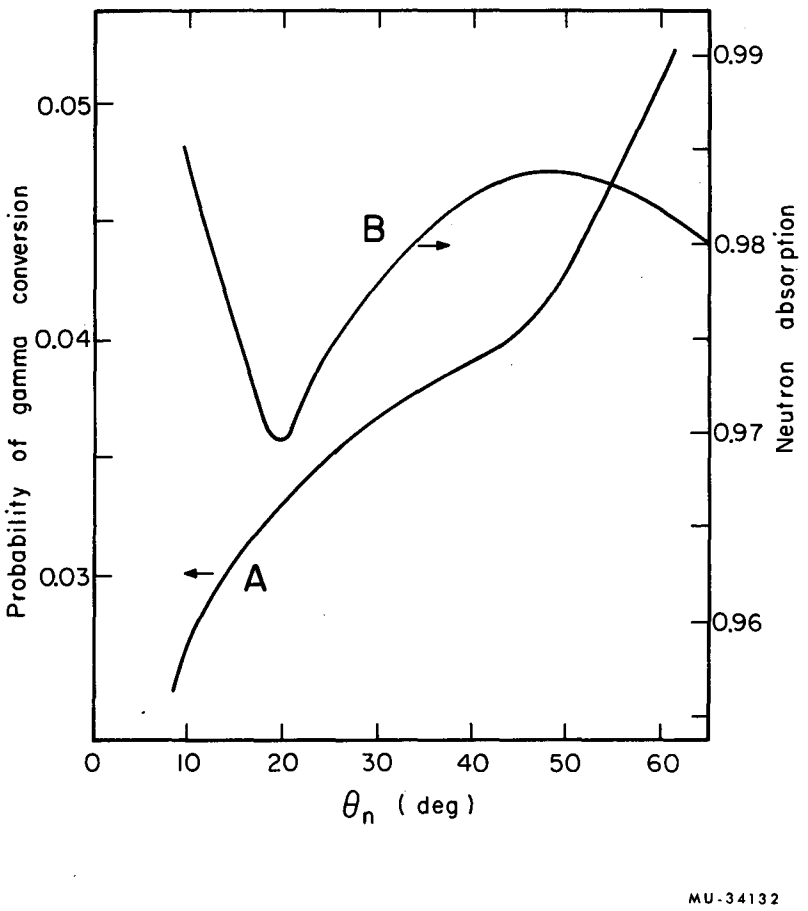

Fig. 13. Gamma conversion and neutron-absorption corrections for T_{π^-} = 313 MeV. Results were similar at 371 MeV. A. Probability that either γ associated with elastic neutrons will convert and register in S_4. B. Fraction of neutron flux not absorbed in target material.

First, a given small fraction of the pions in the tails of the profiles was counted by the monitor system but missed the target. Table IV shows this value for each beam. The neutron yield was adjusted by the reciprocal of the fraction of the pions incident on the target.

Second, because the ends of the liquid hydrogen flask were slightly curved, the effective target length was given by the mean value of the physical flask length weighted by the beam distribution over the cross-sectional area of the target. This was calculated from

$$t_{eff} = \int dr\, d\theta\, r\, f(r)\, g(r,\theta) / \int dr\, d\theta\, r\, g(r,\theta),$$

where $f(r)$ is the physical flask length, $g(r,\theta)$ is the beam distribution function, and r is the distance from the target and beam center line. The integration is, of course, over the cross-sectional area of the flask. Table IV gives this value for each beam energy.

The effective target length is used in computing nt, the number of scatters per cm^2. In this factor, $n = \rho N_0/M$, where N_0 is Avogadro's number and M is the gram atomic weight of hydrogen. Because of gaseous H_2 in the target-empty subtraction, the proper value for ρ is 0.069 g/cm^3. This is the difference between the density of liquid hydrogen and the density of hydrogen gas at liquid nitrogen temperature.[23]

Table IV. Beam-profile corrections.

π^- Beam (MeV)	Fraction of monitored pions incident on target (%)	t_{eff} (in.)
313	96.51	5.731
371	97.46	5.759

6. Radiative Absorption

Neutrons that originate in the radiative absorption reaction (3) cannot be resolved by time of flight, and must be subtracted from the events recorded in the neutral-mode data. The value for this correction can be obtained from a detailed-balance calculation, since radiative absorption is the "complementary" reaction to pion photoproduction,

$$\pi^- + p \rightleftarrows \gamma + n .$$

The differential cross section for the reaction proceeding toward the right is given by

$$\frac{d\sigma}{d\Omega}(\rightarrow) = \left(\frac{P_n}{P_p}\right)^2 \frac{(2S_\gamma)(2S_n + 1)}{(2S_{\pi^-} + 1)(2S_p + 1)} \frac{d\sigma}{d\Omega}(\leftarrow)$$

where P_n and P_p are the center-of-mass momenta; and S_γ, etc. represent the spins of the various particles. The two reactions are compared at the same total center-of-mass energy, and the differential cross sections apply to the same center-of-mass angles. The negative-pion-photoproduction cross section $d\sigma/d\Omega\,(\leftarrow)$, was obtained from the negative-to-positive pion-photoproduction ratio (π^-/π^+) from deuterium as measured by Neugebauer et al.,[24] and the positive-pion-photoproduction cross sections of Walker et al.[25] and Tollestrup et al.[26]

$$\frac{d\sigma}{d\Omega}(\leftarrow) = \left(\frac{\pi^-}{\pi^+}(\theta)\right)\left(\frac{d\sigma}{d\Omega}\right)_{\gamma + p \rightarrow \pi^+ + n}$$

The results obtained from this calculation are shown in Fig. 14, and the neutral-mode data were corrected by a corresponding amount.

C. Cross-Section Calculation

Once the corrected neutron-yield spectra were available for the neutral-mode data, the elastic-neutron peak could be fitted with a Gaussian curve, as indicated in Fig. 11. The area under this curve represented the total-elastic-neutron yield Y for each laboratory angle. The charge-exchange differential cross section could then be calculated from

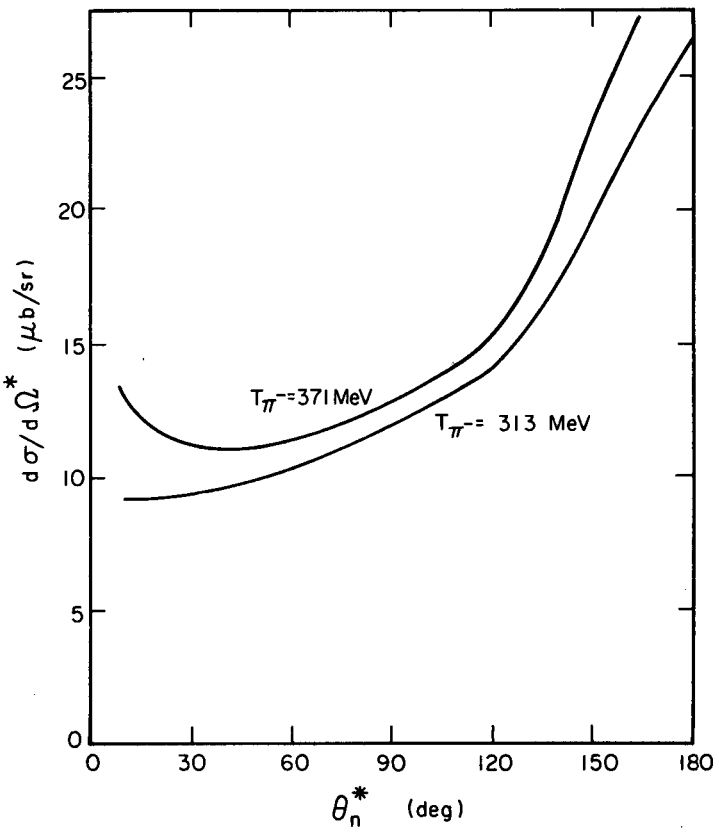

Fig. 14. Radiative absorption. Differential cross section for the production of neutrons from the reaction $\pi^- + p \rightarrow \gamma + n$.

$$\frac{d\sigma}{d\Omega^*} = \frac{Y}{nt\epsilon\Delta d\Omega} \frac{d\Omega}{d\Omega^*}$$

where

* indicates center-of-mass system,
nt = number of scatters per cm^2,
ϵ = neutron-detection efficiency,
$\Delta\Omega$ = solid angle subtended by the neutron detector,
$d\Omega/d\Omega^*$ = center-of-mass solid-angle transformation.

The statistical error in this cross section was completely negligible compared with the uncertainty in the detection efficiency. Therefore this latter value (± 10%) was assigned as the uncertainty in the cross section.

The measured inelastic-neutron distributions in both the neutral mode ($\pi^0\pi^0 n$) and the charged mode ($\pi^+\pi^- n$) could be compared to phase-space distributions and distributions enhanced by an I = 0 two-pion interaction, in either of two ways. The first would be at a constant neutron angle. This would correspond to a vertical cut through the kinematically allowed inelastic area shown in Figs. 15 and 16. In effect, this is what is shown in the inelastic distribution in Fig. 11 except that the abscissa has been plotted as time of flight instead of neutron energy.

The second possibility for comparison is at a constant neutron energy. This corresponds to a horizontal cut through the inelastic neutron areas in Figs. 15 and 16. However in this case an energy band can be selected sufficiently wide to avoid the statistical fluctuations seen in Fig. 11. In addition, since the neutron energy is constant, any inaccuracy in the neutron-detection efficiency is eliminated from the shape of the distribution. Because of these advantages the second presentation was chosen.

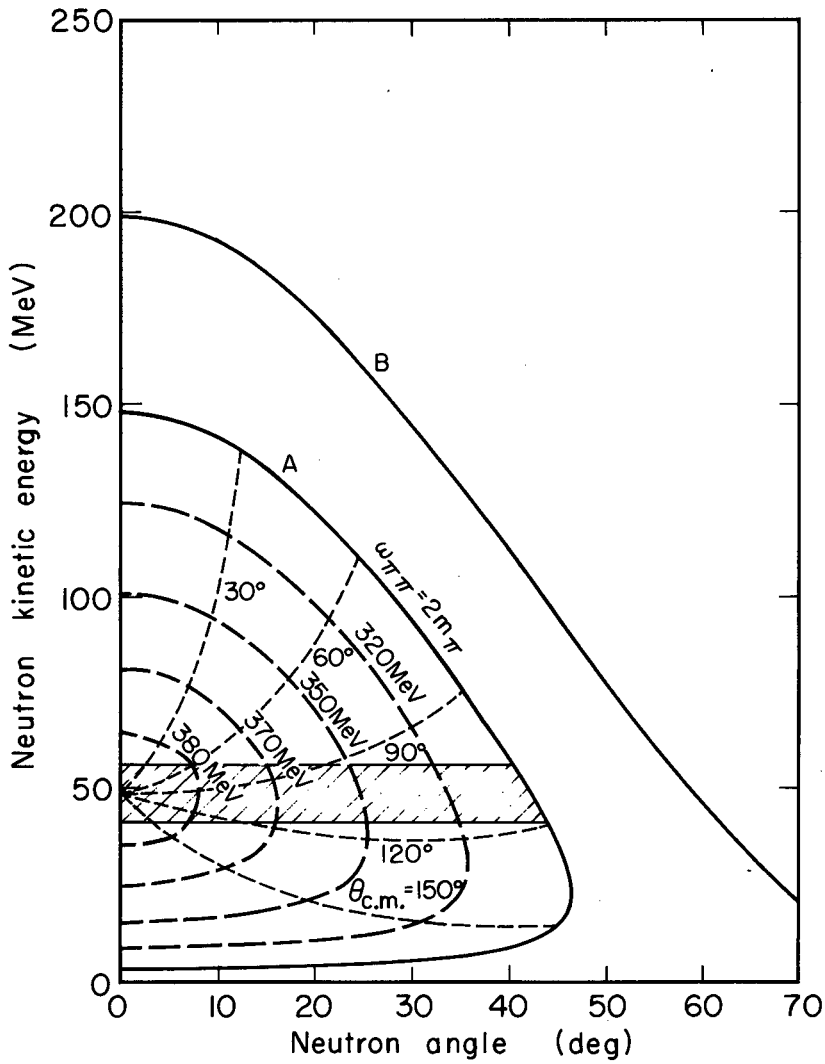

Fig. 15. Laboratory-system neutron kinematics for the processes $\pi^- p \rightarrow \pi\pi n$ (region inside curve A) and $\pi^- p \rightarrow \pi^0 n$ (curve B) at 313 MeV.

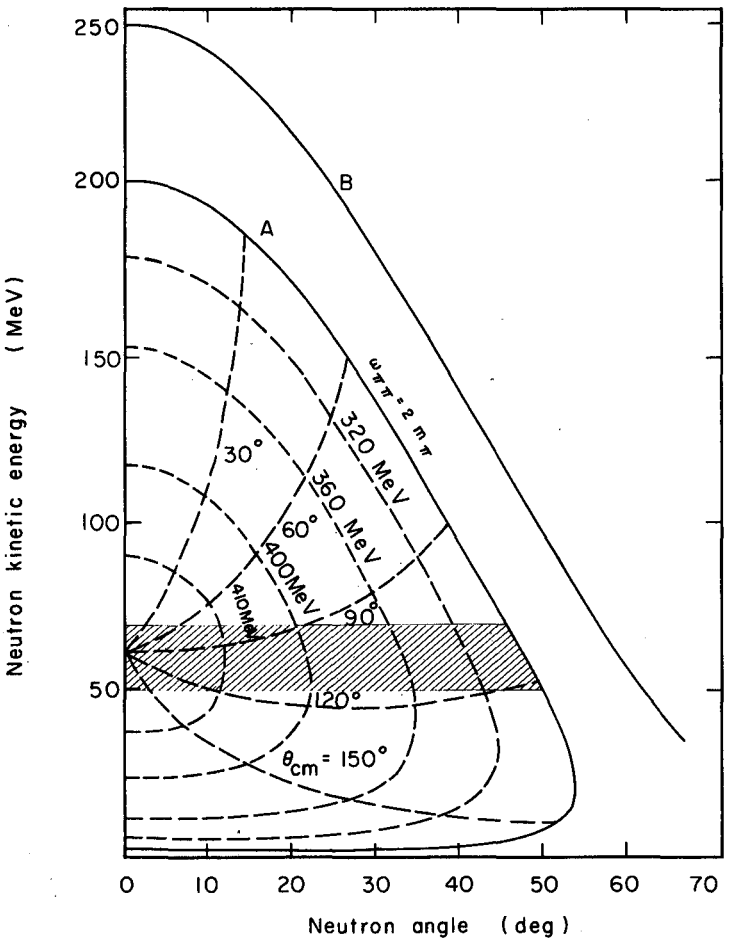

Fig. 16. Laboratory-system neutron kinematics for the processes $\pi^- p \rightarrow \pi\pi n$ (region inside curve A) and $\pi^- p \rightarrow \pi^0 n$ (curve B) at 371 MeV.

For the energy bands indicated in Figs. 15 and 16, we calculated

$$\frac{d^2\sigma}{dT\, d\Omega} = \frac{Y}{nt\epsilon\Delta\Omega\Delta E_n}$$

where Y is now summed over the appropriate PHA channels at each neutron angle, and ΔE_n is the width of the neutron-energy band. The other symbols remain the same as previously defined.

IV. RESULTS

A. Elastic Neutrons

The charge-exchange differential cross section at 313 and 371 MeV, obtained from the calculation in Sec. III.C, is presented numerically in Table V. These data are also presented graphically in Figs. 17 and 18. In addition these figures show neutron differential-cross-section data measured at $T_{\pi^-} = 374$ MeV in the range $84 \leq \theta_n^* \leq 133$ deg,[10] and the differential cross section at $\theta_{\pi^0}^* = 0$ deg calculated from the forward-direction fixed-momentum-transfer dispersion relations for pion-nucleon scattering.[27] For comparison with other work in the field, these results are plotted as a function of the center-of-mass angle of the π^0 meson.

Figures 17 and 18 illustrate the results of a least-squares analysis of this data of the form:

$$\frac{d\sigma}{d\Omega^*}(\cos\theta_{\pi^0}^*) = \sum_{\ell=0}^{N} a_\ell P_\ell(\cos\theta_{\pi^0}^*) .$$

The fourth-order fit to the measured neutron data points (including the Kurz points in Fig. 18) and the dispersion-relation point is shown by the dashed line marked "neutron data." The Legendre coefficients a_ℓ for this analysis are listed in Table VIII. The other two curves in the figures are discussed in Sec. V.

By integration of the $d\sigma/d\Omega^*$ curve over $\cos\theta_{\pi^0}^*$, a value for the total cross section σ_T for the reaction $\pi^- + p \rightarrow \pi^0 + n$ was obtained. These results are presented in Table VI, and are calculated from the "combined" data discussed in Sec. V.

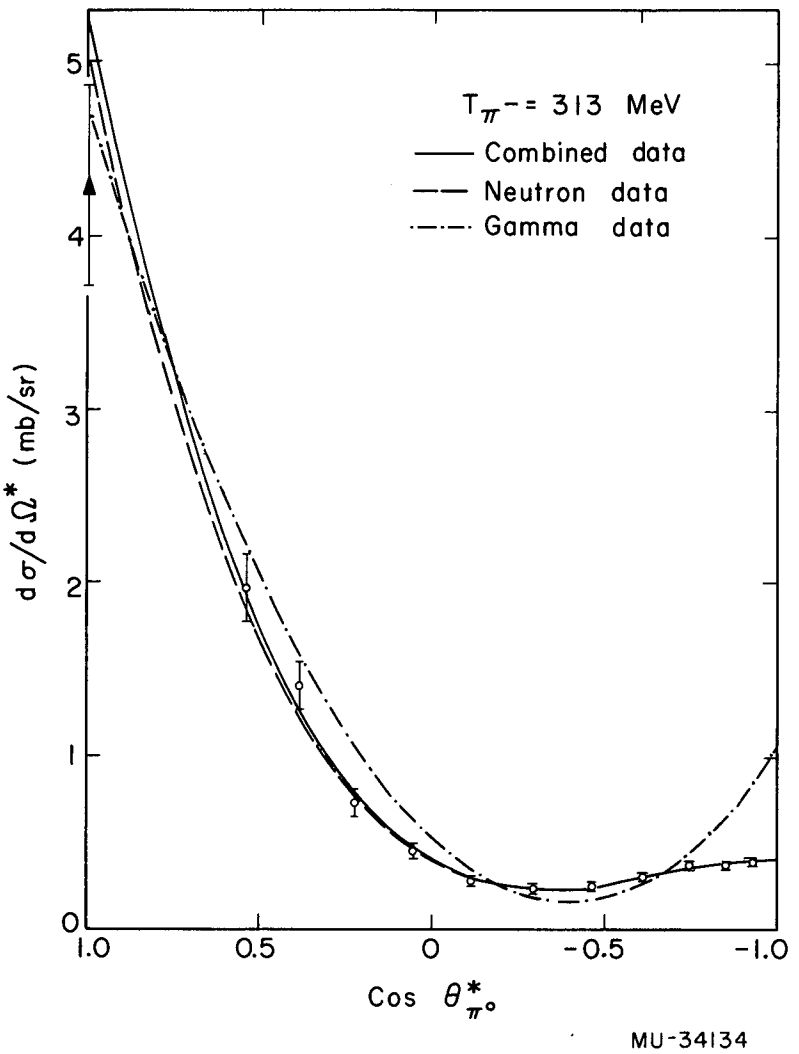

Fig. 17. Charge-exchange differential cross section at T_{π^-} = 313 MeV.

O, Differential cross section measured in this experiment

Δ, Forward-dispersion-relation calculation. (The curves are explained in the text.)

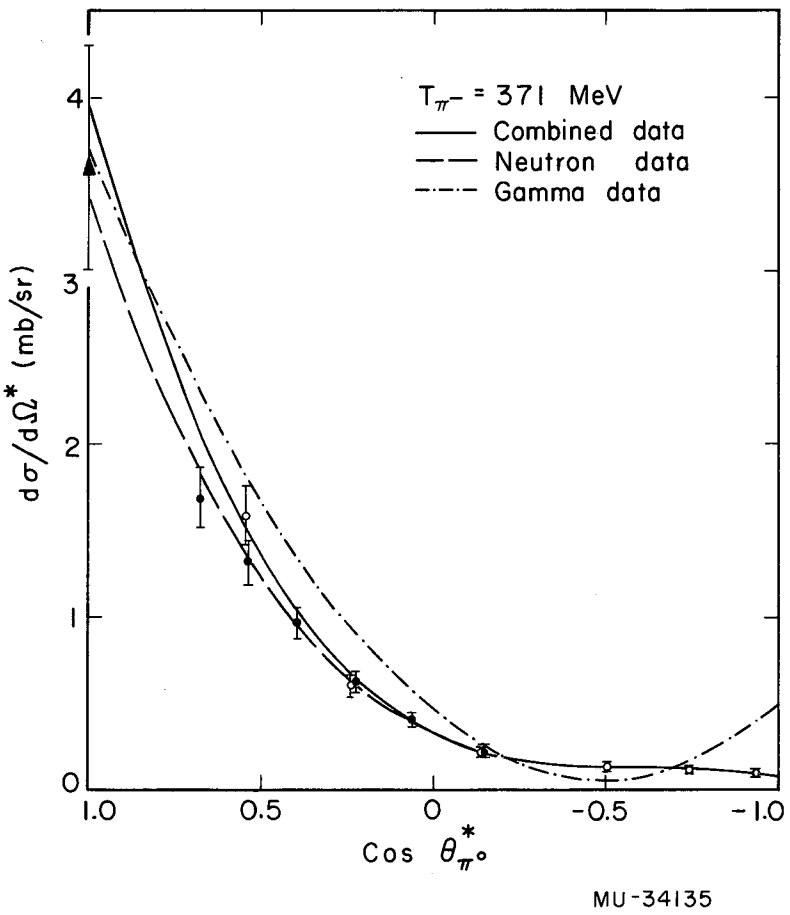

Fig. 18. Charge-exchange differential cross section at T_{π^-} = 371 MeV.

O, Differential cross section measured in this experiment

●, Differential cross section measured by Kurz

Δ, Forward-dispersion-relation calculation.

(The curves are explained in the text.)

Table V. Charge-exchange differential cross section.

θ^*_n (deg)	T_{π^-} = 313 MeV $d\sigma/d\Omega$ (mb/sr)	T_{π^-} = 371 MeV $d\sigma/d\Omega$ (mb/sr)
21.0	0.46±0.10	0.10±0.01
31.5	0.41±0.05	
41.9	0.37±0.04	0.11±0.01
52.2	0.32±0.03	
62.5	0.27±0.03	0.14±0.01
72.7	0.23±0.02	
82.8	0.28±0.03	0.22±0.02
92.8	0.44±0.04	
102.8	0.73±0.07	0.60±0.06
112.7	1.40±0.14	
122.4	1.77±0.20	1.59±0.16

Table VI. Total charge-exchange cross section.

T_{π^-} (MeV)	σ_T (mb)	±
313	15.1	0.4
371	11.1	0.2

B. Inelastic Neutrons

The results of the $d^2\sigma/dT\, d\Omega$ calculation in Sec. II.C for both $\pi^+\pi^-n$ and $\pi^0\pi^0n$ final states are presented numerically in Table VII and graphically in Figs. 19 and 20. Also shown in the figures are the phase-space distribution and the distribution calculated by using an I = 0 two-pion interaction enhancement factor with $a_0 = 2\mu^{-1}$ and R = 0. This value of a_0 is the scattering length tentatively proposed by Abashian et al.[12] for this I = 0 $\pi\pi$ interaction, and R = 0 is the radius of interaction. These curves are normalized to the integral of the distribution for $\pi^+\pi^-n$ over $\cos\theta$.

Table VII. Inelastic neutron $d^2\sigma/dT\ d\Omega$ distribution at constant neutron energy.

T_{π^-} (MeV)	$\cos\theta_n$	$d^2\sigma/dT\ d\Omega(\pi^+\pi^-n)$ (μb/MeV-sr)	$d^2\sigma/dT\ d\Omega(\pi^0\pi^0n)$ (μb/MeV-sr)
313	0.9848	57.3±16.8	
	0.9659		10.9±16.5
	0.9593	33.5± 6.2	
	0.9397		12.7±13.9
	0.9063	16.0± 8.8	8.3±14.0
	0.8660	11.7± 2.7	7.9± 3.9
	0.8192	7.1± 2.7	3.6± 4.0
	0.7660	6.7± 2.6	5.9± 4.3
371	0.9848	60.1±11.0	18.7±10.7
	0.9397	36.4± 5.5	20.0± 7.0
	0.8660	15.2± 3.9	8.9± 4.4
	0.7660	6.0± 2.8	0.4± 4.2

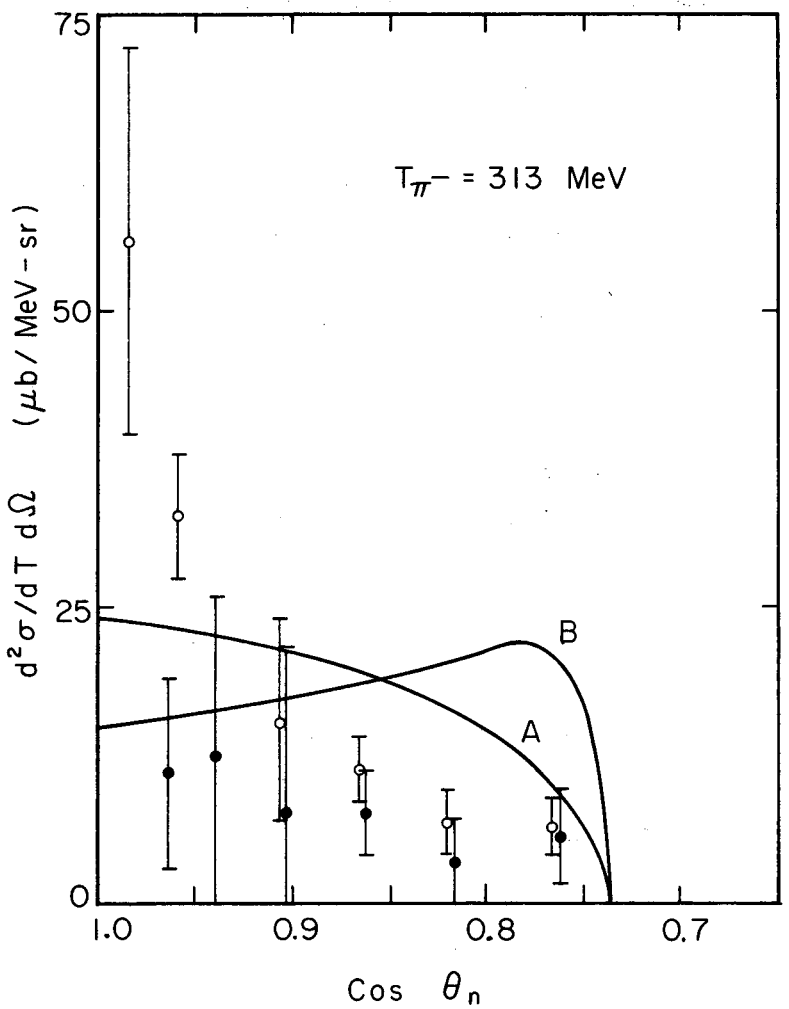

Fig. 19. Inelastic-neutron differential distribution for T_{π^-} = 313 MeV neutron energy interval of 42 to 57 MeV.
O $d^2\sigma/dTd\Omega$ for $\pi^+\pi^-n$; ● $d^2\sigma/dTd\Omega$ for $\pi^0\pi^0n$; A phase-space distribution;
B distribution for I = 0 $\pi\pi$ interaction with $a_0 = 2\mu^{-1}$ and R = 0.

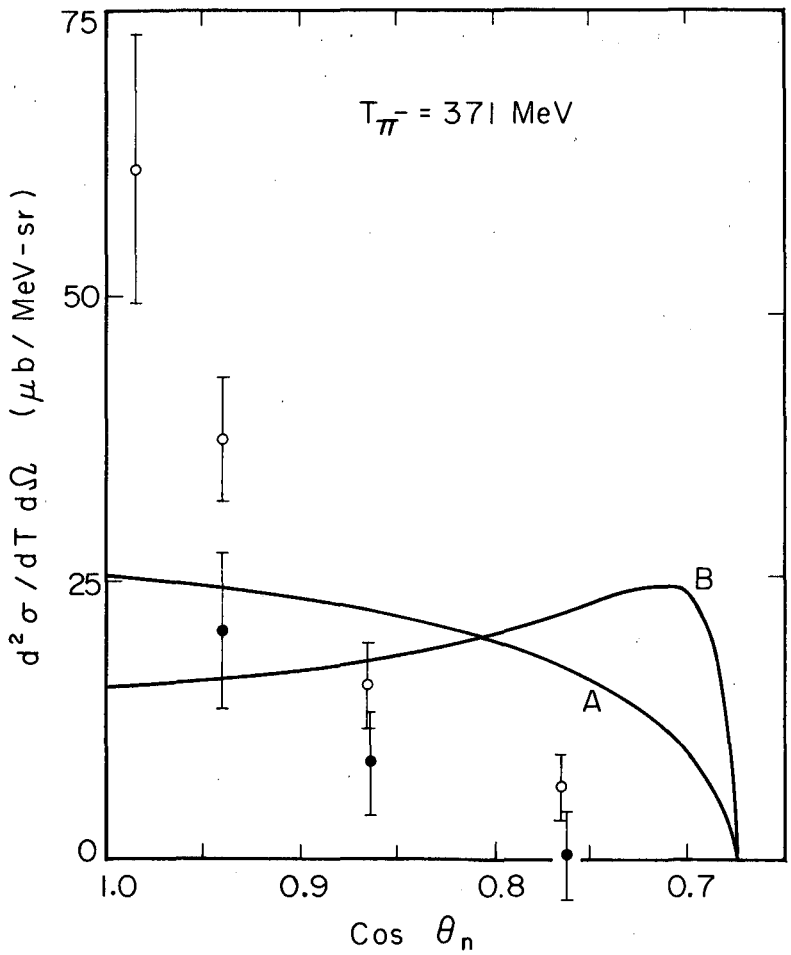

Fig. 20. Inelastic-neutron differential distribution for T_{π^-} = 371 MeV; neutron energy interval of 50 to 69 MeV.
O $d^2\sigma/dTd\Omega$ for $\pi^+\pi^-n$; ● $d^2\sigma/dTd\Omega$ for $\pi^0\pi^0n$; A phase-space distribution;
B distribution for I = 0 $\pi\pi$ interaction with $a_0 = 2^{-1}_{\mu}$ and R = 0.

V. DISCUSSION OF RESULTS

The charge-exchange differential cross section as measured directly from the neutron angular distribution was compared with the cross section as deduced from the gamma-ray angular-distribution measurements by Caris et al.[6] These γ-ray data were incorporated into the least-squares analysis by representing $d\sigma/d\Omega^*$ in a Legendre expansion as in the neutron least-squares analysis. If we follow the procedure of Caris et al. and take into account the γ detection efficiency of the experimental system, the expected γ angular distribution in the center-of-mass system, is given by

$$\frac{d\sigma^{\gamma}}{d\Omega^*}(\cos\theta^*_{\gamma}) = \sum_{\ell=0}^{N} a_{\ell} P_{\ell}(\cos\theta^*_{\gamma}) \int_{-1}^{1} dx \frac{P_{\ell}(x)\epsilon(k)}{(\gamma - \eta x)^2} ,$$

where x is the cosine of the angle between the gamma and the π^0 in the c.m. system; γ and η denote the motion of the π^0 rest system with respect to the c.m. system; and $\epsilon(k)$ is the γ-detector efficiency as a function of the photon lab-system energy k, which in turn is a function of x and $\cos\theta^*_{\gamma}$.

Before the γ-ray data were compared with the neutron data, they were reanalyzed to take into account photons originating from the reactions $\pi^- + p \rightarrow \pi^0 + \pi^0 + n$ and $\pi^- + \pi^0 + p$. The availability of more precise information on these reactions[28] made feasible a more accurate estimate of this correction than was possible in the original analysis by Caris et al.

The present analysis to account for the two-pion final state started with the uncorrected data of Caris et al. (see Table IV of Ref. 6). For each reaction it was assumed that the π^0's had an invariant phase-space energy distribution and an isotropic angular distribution in the c.m. system. We calculated the corresponding lab-system distribution of photons in energy and angle, $d^2\sigma/dk\, d\Omega$, with a normalization determined by the total cross sections for the $\pi^0\pi^0 n$ and $\pi^-\pi^0 p$ reactions. The quantity

$$\frac{d\sigma^{\text{inel.}}}{d\Omega}(\theta_\gamma) = \int dk \; \frac{d^2\sigma(k, \theta_\gamma)}{dk\, d\Omega} \; \epsilon(k)$$

was subtracted from the uncorrected points of the Caris data. We used their original values for the remaining corrections discussed by Caris et al. to obtain the values of $d\sigma^{\gamma}/d\Omega^*$ used in this analysis.

The results of the least-squares analysis of the recorrected γ data are shown by the broken line marked "gamma data" in Figs. 17 and 18. The solid curve was obtained by combining the neutron and gamma data. The neutron data dominate in determing the shape of this curve in the backward π^0 angles (forward neutron angles) where the gamma data are most suspect and have the least statistical weight. Likewise the γ data have the greatest weight in the forward π^0 angles where they are most reliable and where no neutron data were available. We feel that this distribution, therefore, represents the most reliable charge-exchange differential cross section available from presently existing data.

These angular distributions deviate from those determined from the γ data alone in a manner that is in agreement with the predictions of an energy-dependent phase-shift analysis of pion-nucleon scattering by Roper.[29, 30] He used the data of Caris et al. in his analysis, as well as all other available data on pion-nucleon scattering. The predictions of Roper are compared with both the "combined data" and the "gamma data" curves in Fig. 21.

The results of the least-squares analysis are also shown in Table VIII. At both energies the probability of fit was not significantly increased for $N > 2$ when the γ data were analyzed separately. If the neutron data were included, $N = 3$ was required for an acceptable fit. The nonzero value of a_3 is consistent with the requirement of at least D waves in other analysis of pion-nucleon interactions at $T_\pi = 310$ MeV.[7] The behavior of the angular distribution in the region

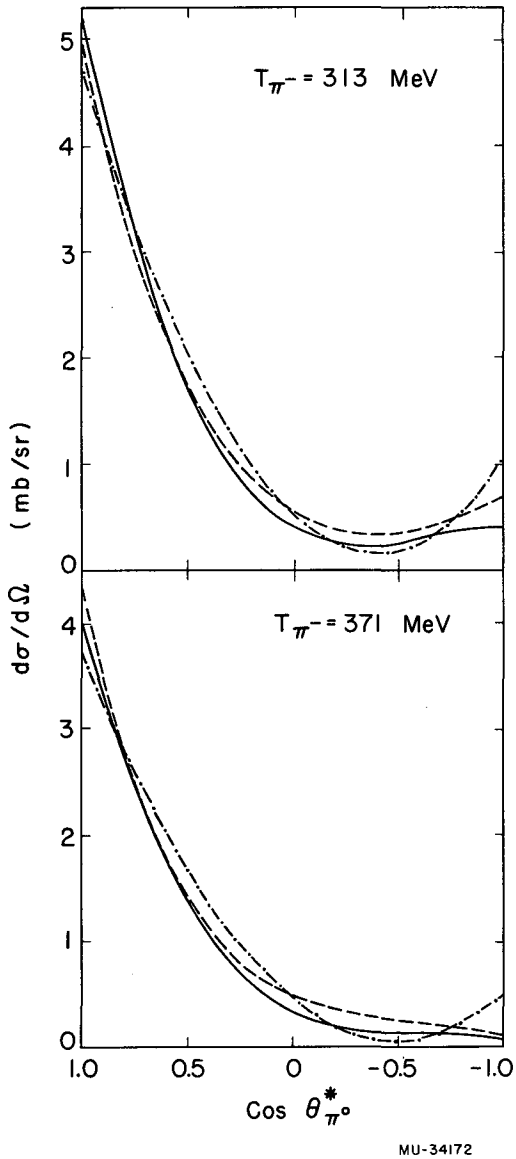

Fig. 21. Comparison of differential cross section.
———combined data; — · — gamma data;
— — — differential cross section predicted
by Roper phase-shift solutions.

Table VIII. Results of the least-squares fits of the form

$$d\sigma/d\Omega^*(\cos\theta^*_{\pi^0}) = \sum_{\ell=0}^{N} a_\ell P_\ell(\cos\theta^*_{\pi^0})$$

to the differential cross section for $\pi^- + p \rightarrow \pi^0 + n$.

T_{π^-} (MeV)	Footnote	N	a_0 (mb/sr)	a_1 (mb/sr)	a_2 (mb/sr)	a_3 (mb/sr)	Probability of fit
313	a	2	1.31±0.04	1.86±0.08	1.57±0.11	-	0.57
	b	2	0.92±0.04	1.17±0.08	0.96±0.07	-	10^{-3}
		3	1.13±0.06	1.73±0.14	1.50±0.13	0.44±0.09	0.88
	c	2	1.16±0.03	1.62±0.05	1.31±0.05	-	$<10^{-4}$
		3	1.21±0.03	1.88±0.06	1.61±0.06	0.45±0.06	0.40
371	a	2	1.00±0.03	1.62±0.06	1.12±0.08	-	0.15
	b	2	0.60±0.02	0.89±0.05	0.44±0.03	-	$<10^{-4}$
		3	0.80±0.03	1.37±0.08	0.96±0.07	0.31±0.04	0.75
	c	2	0.77±0.02	1.26±0.03	0.67±0.02	-	$<10^{-4}$
		3	0.89±0.02	1.57±0.04	1.13±0.04	0.38±0.03	0.12

a. γ data only.

b. Neutron data and forward-direction dispersion-relation point.

c. All data combined.

of $\theta^*_{\pi^0} = 180$ deg is not consistent with any of the SPD solutions of Vik and Rugge. Figure 2 of Ref. 7 shows the Caris distribution at backward π^0 angles below the SPD predictions for the charge-exchange differential cross section. At these same angles, the distribution we measure is below that of Caris, i.e., even further from the SPD predictions. (The measurements[31] of the charge-exchange neutron polarization at $T_{\pi^-} = 310$ MeV are also inconsistent with the SPD solutions.) Instead, the differential cross section that we obtained corresponds more closely to predictions obtained from SPDF solutions II and IV of Vik and Rugge.[29] The SPDF solution II is also preferred by Donnachie et al. in their theoretical analysis of pion-nucleon scattering.[32]

The distribution of inelastic neutrons from the $\pi^+\pi^-n$ final state as shown in Figs. 19 and 20 departs noticeably from both the phase-space distribution and the ABC enhancement distribution. We observe that there is a strong peaking at low c.m. energy for the neutron. This same effect was observed by Kirz et al.,[13] Barish et al.,[28] and Blokhintseva et al.[33] These low-neutron energies correspond to a dipion effective mass in the range (near $m_{\pi\pi} = 400$ MeV) where several authors report I = 0 two-pion resonances.[34-36] This low-energy peaking seems to be present at $T_{\pi^-} = 371$ MeV in the $\pi^0\pi^0n$ distribution, which is in agreement with Barish et al. but is not clearly evident at 313 MeV. However the large statistical errors do not justify firm conclusions.

The enhancement of the distribution from an I = 0 two-pion interaction, which has been proposed to explain the anomaly observed by Abashian et al.,[12] is not observed. However the domination of the distribution by a strong enhancement at the opposite end of the neutron-c.m.-energy range may mask this effect. Finally we note that an explanation has been proposed by Anisovich and Dakhno for both of these enhancements in terms of a singularity in the scattering amplitude.[37]

ACKNOWLEDGMENTS

It is a pleasure to express my appreciation to Professor Burton J. Moyer for his continuing interest and guidance in this research. I would like to thank Dr. Victor Perez-Mendez for his advice and supervision throughout this experiment.

I am also indebted to Dr. Philip M. Ogden and Dr. Barry C. Barish for their aid in preparing and running the experiment; to Dr. Julius Solomon for his assistance in the beam-optics calculations; and to Dr. Richard J. Kurz, both for his helpful advice in analyzing the data and for his prior developmental work in this experimental technique.

I would like to thank James T. Vale and the cyclotron crew and Robert E. Walton and the accelerator technicians for their cooperation during the course of the experimental work; and Miss Miriam L. Machlis for her cooperative and diligent secretarial assistance.

Finally I would like to express my eternal gratitude to my wife, Kathleen, for her patience in managing a household of five children during the long gestation period of this dissertation.

This work was done under the auspices of the U. S. Atomic Energy Commission.

APPENDICES

A. Gamma-Conversion Calculation

We desire to calculate the total probability that either of the two π^0-decay γ rays associated with a charge-exchange neutron will convert by pair production in the material surrounding the liquid hydrogen target and thus register in the S_4 scintillation counter. This is to be calculated as a function of the laboratory angle of the associated neutron.

First we set the incident energy T_{π^-} for the original charge-exchange reaction, $\pi^- + p \rightarrow \pi^0 + n$. We can then calculate β, γ, and η, where

β = the velocity of the c.m. system observed in the lab system,

$\gamma = (1-\beta^2)^{-1/2}$,

$\eta = \beta\gamma$,

and the corresponding values β_0, γ_0 and η_0 for the π^0 rest system as observed in the c.m. system.

Next we designate a particular neutron lab angle θ_n, and calculate the corresponding c.m. angle θ_n^* (* denotes a c.m.-system angle). This angle, $\theta_n^* = \theta_0^* - \pi$, where θ_0^* is the polar angle of the π^0 and ϕ_0^*, is defined as 0 deg. Let $x_0 = \cos\theta_0^*$ and $y_0 = \sin\theta_0^*$.

Now let θ and ϕ represent the direction of the γ ray in the lab system; and $x = \cos\theta$ and $y = \sin\theta$. We can calculate the polar angle θ^* of the γ ray from

$$x_1 = \cos\theta^* = \frac{\gamma x - \eta}{\gamma - \eta x}$$

$$y_1 = \sin\theta^* = \frac{y}{\gamma - \eta x} \quad .$$

Let θ_2^* represent the angle between the π^0 and the γ ray. Then

$$x_2 = \cos\theta_2^* = x_1 x_0 + y_1 y_0 \cos\phi$$

and the γ-ray lab energy k is given by

$$k = \frac{\mu}{2} \frac{1}{(\gamma - \eta x)(\gamma_0 - \eta_0 x_2)}$$

where μ is the π^0 rest mass.

With these kinematic values available we can proceed to the main portion of the calculation. The γ-ray penetration probability ϵ is given by

$$\epsilon = \int d\Omega \left(\frac{d\sigma}{d\Omega^0}\right) \left(\frac{d\Omega^0}{d\Omega}\right) \exp\left[-\sum_i Z_i(\theta)\,\mu_i(k)\right]$$

where

$d\Omega^0$ = the solid angle in the π^0 rest system

$d\Omega$ = the solid angle in the lab system

Z_i = amount of material i in the direction θ

μ_i = mass absorption coefficient for material i.

With two γ rays emitted isotropically in the π^0 rest system, the probability of a single γ ray's being emitted into $d\Omega^0$ is

$$\frac{d\sigma}{d\Omega^0} = 2\left(\frac{1}{4\pi}\right) .$$

The solid-angle transformation is

$$\frac{d\Omega^0}{d\Omega} = \left(\frac{2k}{\mu}\right)^2 .$$

This leaves the following integration to be performed for our particular configuration of target materials, and at each neutron angle θ:

$$2\epsilon = \frac{1}{2\pi}\int_{-1}^{1}\int_{0}^{2\pi} dx\, d\phi \left(\frac{2k}{\mu}\right)^2 \exp\left[-\sum_i Z_i(\theta)\mu_i(k)\right] .$$

The symbol ϵ represents the probability of one γ ray's not converting. The probability that a γ ray will convert is $1 - \epsilon$, and the probability that either of the two γ rays will convert is

$$P_\gamma = 2(1-\epsilon) .$$

The values of P_γ obtained from this calculation are shown in Fig. 13.

B. Neutron-Absorption Calculation

With the kinematic values from Appendix A, it is a relatively straightforward matter to compute the amount of absorption of the neutron flux in the hydrogen-target material as a function of neutron laboratory angle.

The fraction of neutrons transmitted through the target material f_n at each angle θ is

$$f_n = \exp\left[-\sum_i \sigma_i(T_n)\left[nt(\theta)\right]_i\right]$$

where $\left[nt(\theta)\right]_i$ is the number of nuclei per cm^2 for element i, and $\sigma_i(T_n)$ is the absorption cross section for this nuclei as a function of neutron lab kinetic energy T_n. This cross section is well approximated for the C, O, and Al of this target by

$$\sigma_i = \sigma_a A^{2/3} ,$$

where σ_a is an absorption cross section per nucleon for light nuclei, obtained from the Al and C cross section as compiled by Hughes and Schwartz.[38]

The results of this calculation are shown in Fig. 13.

REFERENCES

1. J. Foote, O. Chamberlain, E. Rogers, H. Steiner, C. Wiegand and T. Ypsilantis, Phys. Rev. 122, 948 (1961).
2. E. H. Rogers, O. Chamberlain, J. Foote, H. Steiner, C. Wiegand, and T. Ypsilantis, Rev. Mod. Phys. 33, 356 (1961).
3. V. Zinov and S. Korenchenko, Soviet Phys. --JETP (English transl.) 11, 794 (1960).
4. I. M. Vasilevskiĭ and V. V. Vishnyakov, Soviet Phys. --JETP (English transl.) 11, 323 (1960).
5. Hugo R. Rugge and Olav T. Vik, Phys. Rev. 129, 2300 (1963).
6. J. C. Caris, R. W. Kenney, V. Perez-Mendez, and W. A. Perkins, Phys. Rev. 121, 893 (1961).
7. Olav T. Vik and Hugo R. Rugge, Phys. Rev. 129, 2311 (1963).
8. H. L. Anderson, E. Fermi, R. Martin, and D. E. Nagle, Phys. Rev. 91, 155 (1953).
9. Walton A. Perkins, III, John C. Caris, Robert W. Kenney, and Victor Perez-Mendez, Phys. Rev. 118, 1364 (1960).
10. Richard J. Kurz, Differential Distributions of Neutrons in Inelastic π^-p Interactions at 374, 417, and 454 MeV (Ph. D. Thesis), UCRL-10564, Nov. 1962.
11. Alexander Abashian, Norman E. Booth, and Kenneth M. Crowe, Phys. Rev. Letters 5, 258 (1960); Norman E. Booth, Alexander Abashian, and Kenneth M. Crowe, Phys. Rev. Letters 7, 35 (1961).
12. Alexander Abashian, Norman E. Booth, Kenneth M. Crowe, Roger E. Hill, and Ernest H. Rogers, Phys. Rev. 132, 2296; 2305; 2309; 2314 (1963).
13. Janos Kirz, Joseph Schwartz, and Robert D. Tripp, Phys. Rev. 130, 2481 (1963).
14. Joe Good, Morris Pripstein, and Howard S. Goldberg, CYCLOTRON ORBITS: A 709 Ray-Trace Program for Cylindrically Symmetric Magnetic Fields, UCRL-11044, Oct. 1963.
15. Thomas J. Devlin, OPTIK: An IBM 709 Computing Program for the Optics of High-Energy Particle Beams, UCRL-9727 Sept. 1961.

16. Owen Chamberlain, Optics of High Energy Beams, Ann. Rev. Nucl. Sci. 10, 161 (1960).
17. Julius Solomon and Sypko W. Andreae, Beam-Profile Detector, Rev. Sci. Instr. 34, 1126 (1963).
18. Barry C. Barish, A Study of the Reaction $\pi^- + p \rightarrow \pi^- + \pi^0 + p$ at 310 and 377 MeV (Ph. D. Thesis) UCRL-10470, Aug. 1962.
19. Lawrence Radiation Laboratory Counting Handbook, Lawrence Radiation Laboratory Report UCRL-3307 Rev., Jan. 1959.
20. Arthur E. Bjerke, Quentin A. Kerns, and Thomas A. Nunamaker, Pulse Shaping and Standardizing of Photomultiplier Signals for Optimum Timing Information Using Tunnel Diodes, UCRL-9838, Aug. 1961.
21. Richard J. Kurz, A 709/7090 Fortran II Program to Compute the Neutron-Detection Efficiency of Plastic Scintillator for Neutron Energies from 1 to 300 MeV, UCRL-11339, March 1964.
22. Clyde E. Wiegand, Tom Elioff, William B. Johnson, Leonard B. Auerbach, Joseph Lach, and Thomas Ypsilantis, Detection Efficiency of Plastic Scintillator for Neutron Energies 4 to 76 MeV, UCRL-9986, Dec. 1961.
23. Dudley B. Chelton and Douglas B. Mann, Cryogenic Data Book, UCRL-3421, May 1956.
24. Gerry Neugebauer, Walter Wales, and R. L. Walker, Phys. Rev. 119, 1726 (1960).
25. R. L. Walker, J. G. Teasdale, V. Z. Peterson, and J. A. Vetto, Phys. Rev. 99, 210 (1955).
26. A. V. Tollestrup, J. C. Keck, and R. M. Worlock, Phys. Rev. 99, 220 (1955).
27. David Cheng (Lawrence Radiation Laboratory, Berkeley), private communication, 1964.
28. Barry C. Barish, Richard J. Kurz, Victor Perez-Mendez, and Julius Solomon, Inelastic π^--p Interactions in the Energy Range of 310 to 454 MeV, Phys. Rev. (to be published).
29. L. David Roper (Lawrence Radiation Laboratory, Livermore) private communication, 1964.

30. L. David Roper, Phys. Rev. Letters 12, 340 (1964).

31. Roger E. Hill, Norman E. Booth, Robert J. Esterling, David L. Jenkins, Norman H. Lipman, Hugo R. Rugge, and Olav T. Vik, Bull. Am. Phys. Soc. 9, 410 (1964).

32. A. Donnachie, J. Hamilton, and A. T. Lea, Prediction of p-, d-, and f-Wave Pion-Nucleon Scattering, Phys. Rev. (to be published).

33. T. D. Blokhintseva, , V. G. Grebinnik, V. A. Zhukov, G. Libman, L. L. Nemenov, G. I. Selivanov, and Y. Jung-Fang, Soviet Physics--JETP (English Transl.) 17, 80 (1963).

34. N. P. Samios, A. H. Backman, R. M. Lea, T. E. Kalogeropoulos, and W. D. Shepard, Phys. Rev. Letters 9, 139 (1962).

35. R. Del Fabbra, M. DePretis, R. Jones, G. Marini, A. Odian, G. Stoppini, and L. Tau, Phys. Rev. Letters 12, 674 (1964).

36. C. Richardson, R. Kraemer, M. Meer, N. Nussbaum, A. Persner, R. Strand, T. Toohig and M. Block, Two-Pion Resonances Below Mass 900 MeV, in Proceedings of the International Conference on High-Energy Nuclear Physics, Geneva, 1962, I. Prentki, Ed. (CERN, Scientific Information Service, Geneva, Switzerland, 1962), p. 96.

37. V. V. Anisovich and L. G. Dakhno, Phys. Rev. Letters 10, 221 (1964).

38. Donald J. Hughes and Robert B. Schwartz, Neutron Cross Sections, Brookhaven National Laboratory Report BNL-325, July 1958.